Icarus 376 (2022) 114853

Contents lists available at ScienceDirect

Icarus

journal homepage: www.elsevier.com/locate/icarus

Research Paper

A numerical model of convective heat transfer in Titan's subsurface ocean

Jakub Kvorka *, Ondřej Čadek

Charles University, Faculty of Mathematics and Physics, Department of Geophysics, V Holešovičkách 2, 180 00 Praha 8, Czech Republic

ARTICLE INFO

Keywords:
Titan
Ocean dynamics
Thermal convection
Heat flux variations

ABSTRACT

It has been suggested that the long-wavelength topography of Titan is related to lateral variations in the heat flux from the ocean. Recent studies of the heat transfer in Titan's ocean agree that the time-averaged heat flux can vary in latitude by tens of percent, but they predict different distributions of heat flux anomalies at the upper boundary of the ocean. In order to clarify this issue, we perform 115 numerical simulations of thermal convection in a rotating spherical shell, varying the mechanical boundary conditions and dimensionless input parameters (Rayleigh, Ekman and Prandtl numbers) by at least one order of magnitude. The results of the simulations are examined in terms of the modified transitional number, $R_G^* = RaEk^{12/7}Pr^{-1}$. Depending on the relative importance of rotation, the heat flux maximum is located either at the equator (equatorial cooling) or at the poles (polar cooling). We demonstrate that equatorial cooling occurs when $R_G^* < 1$ or $R_G^* > 10$ while polar cooling occurs when $R_G^* \in \langle 1, 10 \rangle$. Based on this result, we predict that Titan's ocean is in the polar cooling mode and the heat flux distribution is controlled by zonal degree 2 and 4 harmonics. The predicted heat flux shows a high degree of similarity with the axisymmetric part of Titan's long-wavelength topography, indicating a strong relationship between ocean dynamics and the processes in the ice shell.

1. Introduction

Several moons of the giant planets are thought to have liquid-water oceans buried beneath their icy crusts (Nimmo and Pappalardo, 2016). These oceans transport heat and chemicals from the deep interior to the surface, influence the tectonic evolution of the ice crust and are possible candidates for hosting life. Understanding the dynamics of subsurface oceans is therefore critical for comprehending the evolution of icy bodies and evaluating their habitability.

The subsurface oceans are inaccessible to direct observation, but they can be studied by numerical simulations. The simulations are carried out by solving the conservation equations for mass, momentum and energy applied to a rotating viscous fluid (see Appendix A for details). The main drawback of this approach is the order of magnitude difference between the actual values of the parameters that control the real ocean and those that can be achieved in numerical simulations. For example, in numerical simulations of thermal convection in planetary interiors, the Ekman number (Ek, the ratio of viscous to Coriolis forces) is usually five to ten orders of magnitude larger than its real value, while the Rayleigh number (Ra, the ratio of the thermal diffusion time to the viscous buoyant rise time) is usually ten to fifteen orders of magnitude smaller than that expected in natural systems. In spite of this limitation, numerical simulations can provide valuable insight into the dynamics of rotating convective systems since the results obtained for unrealistic Ekman and Rayleigh numbers can be extrapolated using scaling laws. This approach has been used for several decades to investigate magnetic fields generated in molten planetary cores (see, e.g., Roberts and King (2013) for a review) and can also be applied to subsurface oceans of icy moons (e.g. Soderlund et al., 2014; Soderlund, 2019; Amit et al., 2020).

Recent progress in computational algorithms (Schaeffer, 2013) together with increasing computational power have considerably widened the range of accessible Ekman and Rayleigh numbers and made it possible to test theoretical scaling laws and establish "empirical" scalings. Assuming a shell with an inner to outer radius ratio of 0.6, no-slip boundary conditions and gravity proportional to r^{-2}, Gastine et al. (2016) found five different scaling regimes: conductive, weakly nonlinear, rapidly rotating, transitional and non-rotating. Cheng et al. (2018) combined numerical simulations, laboratory experiments and asymptotic predictions and proposed a similar classification but using different terminology to describe the heat transfer modes (subcritical, columnar, plumes, geostrophic turbulence, unbalanced boundary layers, and non-rotating heat transfer). The classifications by Gastine et al. (2016) and Cheng et al. (2018) have been used as the basis for two studies investigating the spatial variations in the heat flux at the upper boundary of a subsurface water ocean (Soderlund, 2019; Amit et al., 2020). Latitudinal variations in heat flux from the ocean have been

* Corresponding author.
E-mail addresses: jakub.kvorka@mff.cuni.cz (J. Kvorka), ondrej.cadek@mff.cuni.cz (O. Čadek).

https://doi.org/10.1016/j.icarus.2021.114853
Received 12 April 2021; Received in revised form 10 December 2021; Accepted 13 December 2021
Available online 1 January 2022

proposed to have contributed to the formation of chaos terrains on Europa (Soderlund et al., 2014), polar depressions on Titan (Kvorka et al., 2018) and ice thickness variations on Enceladus (Čadek et al., 2019b), and are likely to have played a significant role in the evolution of icy moons.

Soderlund (2019) and Amit et al. (2020) show that, depending on the relative importance of rotation, convection models predict three different cooling patterns: (i) the polar cooling, characterized by efficient heat transfer at high latitudes, (ii) the equatorial cooling, characterized by the maximum heat transfer near the equator, or (iii) the uniform cooling, corresponding to convection systems that are not affected by rotation. The studies agree that the lateral heat flux variations may be significant (up to $\sim 50\%$), but their results are contradictory. Whereas the model of Soderlund (2019) predicts the transition from equatorial to polar cooling with increasing influence of rotation, the model by Amit et al. (2020) indicates the opposite trend — the transition from polar to equatorial cooling. It is therefore difficult to draw conclusions about the cooling patterns relevant to icy moon oceans because the two sets of results do not allow a unique interpretation.

The study of Amit et al. (2020) focuses on Titan where the variations of oceanic heat flux have been estimated from analysis of topographic data (Kvorka et al., 2018). Amit et al. (2020) classify the heat transfer regime in Titan's ocean as transitional to non-rotating and argue for enhanced polar cooling, which contrasts with the results of Soderlund (2019) suggesting weak equatorial cooling in this regime. This discrepancy may be related to differences in geometry and boundary conditions, or to the way in which the results are extrapolated to the real world. In both studies, convection is driven by a fixed temperature contrast between the inner and outer boundary, but the results presented by Soderlund (2019) are obtained for a radius ratio of 0.9 and free-slip boundary conditions, while the numerical simulations discussed in Amit et al. (2020) are performed for a radius ratio of 0.8 and no-slip boundary conditions.

In macro-scale applications, no-slip is the proper boundary condition for a viscous fluid at a rigid boundary. Since the subsurface ocean is treated as a fluid shell with rigid and impermeable boundaries, the no-slip boundary condition seems to be the correct choice. However, as pointed out by Kuang and Bloxham (1997), the use of the no-slip condition may be problematic because the Ekman number used in numerical models is many orders of magnitude larger than in the real fluid. As a consequence, no-slip models tend to overestimate viscous effects, resulting in a thick Ekman layer (the boundary layer in which the frictional force is balanced by the Coriolis force). Since the net torque acting on the fluid shell is generally not equal to zero, the no-slip boundary conditions lead to a differential rotation of the ocean with respect to the ice crust and the silicate core. In contrast, the free-slip boundary condition effectively reduces the Ekman layer thickness to zero, and since there is no viscous coupling across the boundaries, the total angular momentum of the ocean is conserved (see also Kuang and Bloxham, 1999). The absence of friction forces in free-slip models is accompanied by the development of strong zonal flows, possibly influencing the heat transport in the ocean.

Current computational power does not allow numerical simulations of thermal convection with realistic Ekman and Rayleigh numbers. To avoid this problem, Soderlund (2019) and Amit et al. (2020) have performed a series of numerical simulations with parameters that are computationally tractable and interpreted the results using a scaling analysis. There are two problems that make it difficult to extrapolate the results of convection simulations to the real world. First, we do not know the superadiabatic temperature difference, ΔT, across the ocean. Given that $Ra \propto \Delta T$, this means that the Rayleigh number of the real ocean cannot be determined directly from the definition. Since the total heat output of the convective system is usually known, several methods have been proposed to estimate the Rayleigh number from the Nusselt number, Nu, characterizing the total heat transfer across the fluid domain. Soderlund (2019) and Amit et al. (2020) estimated the interval of possible values of Ra using the scaling laws for two end member cases: a rapidly rotating ocean and a non-rotating ocean (Gastine et al., 2015, 2016).

The second problem consists of finding the relationship between the numerical simulations performed for unrealistic values of control parameters and the real system, i.e. of determining the properties of the real system from the results of the numerical modeling. This can be done using a convective regime diagram (see, e.g., Fig. 1 in Soderlund (2019) or Fig. 10 in Amit et al. (2020)). The implicit assumption behind this approach is that each convective regime has its own specific cooling pattern. This assumption is likely to be satisfied for rapidly rotating convective systems but it may not be valid in the case of the transitional regime where the heat flux pattern does not show a clear trend (Amit et al., 2020). It is also worth mentioning that the convective regime diagrams themselves are uncertain to some extent since they can use different scaling laws to describe the same transition. For example, the transition to the non-rotating regime can be described by either the convective Rossby number ($\propto Ek$) or the transitional number R_G ($\propto Ek^{12/7}$, see Table 2), which however differ by orders of magnitude at Ekman numbers relevant to ocean worlds (see red-shaded area in Fig. 1 of Soderlund (2019)). Another problem is that the empirical scaling relations are mostly based on numerical simulations with a radius ratio of 0.6 or smaller while the ratio of the inner to outer radius of a subsurface ocean is typically greater than 0.8.

Alternatively, one can characterize the system using a suitable 'diagnostic' parameter. This parameter must be sensitive to changes in the heat flux pattern, insensitive to order-of-magnitude changes in control parameters Ek and Ra, and must be chosen such that the heat flux characteristics can be unambiguously expressed in terms of this parameter. This approach was used by Amit et al. (2020) who analyzed the dependence of the heat flux characteristics on two diagnostic parameters: the local convective Rossby number, Ro_{loc}, and the transitional Rayleigh number, R_T (for the definitions, see Eqs. (15) and (16) in Amit et al. (2020)).

The purpose of this paper is to clarify the discrepancy between the results of Soderlund (2019) and Amit et al. (2020) and to estimate the distribution of the heat flux coming from Titan's subsurface ocean. To resolve this issue we perform a series of numerical simulations in 3d spherical geometry in which we vary Rayleigh, Ekman and Prandtl numbers (Prandtl number, Pr, is the ratio of momentum diffusivity to thermal diffusivity) and change the mechanical boundary conditions. The results of these simulations are interpreted in terms of different diagnostic parameters and used to estimate the Rayleigh number of Titan's ocean. In particular, we attempt to answer the following two questions: (i) What is the most appropriate parameter for the classification of cooling patterns in convective systems weakly affected by rotation? (ii) How much is the extrapolation of the numerical models affected by the choice of the mechanical boundary condition? Answering these questions is essential for understanding the heat transfer in subsurface oceans of icy moons and the role it plays in the thermo-mechanical evolution of the ice crust.

2. Control and diagnostic parameters

The heat and mass transfer in the ocean is controlled by three dimensionless parameters: the Rayleigh, Ekman and Prandtl numbers (see Appendix A for details). The values of the control parameters appropriate to Titan's ocean are given in the third column of Table 1. While the Ekman and Prandtl numbers can easily be calculated using the formulas in Table 1, the accurate determination of the Rayleigh number is difficult since we do not know the superadiabatic temperature contrast ΔT in the subsurface ocean. This problem can be circumvented by using the total heat flow in combination with a scaling law that relates the control parameters to the Nusselt number (the ratio of total to conductive heat transfer across the ocean). The issue of

Table 1
Parameters controlling heat and mass transfer in the ocean. Here, α denotes the thermal expansivity, g_o is the gravitational acceleration at the outer boundary, ΔT is the superadiabatic temperature contrast between the boundaries, D is the thickness of the ocean, κ is the thermal diffusivity, ν is the kinematic viscosity, and Ω is the rate of rotation. The values of Ra and Ek in the third column correspond to Titan where the thickness of the ocean is estimated to be between 100 and 500 km (see Table B.3). The scaling used to determine the Rayleigh number is discussed in Appendix B.

Parameter	Definition	Value on Titan	This study
Rayleigh number (Ra)	$\alpha g_o \Delta T D^3/(\kappa\nu)$	$4 \cdot 10^{19} - 9 \cdot 10^{21}$	$2.1 \cdot 10^6$–$3.8 \cdot 10^7$
Ekman number (Ek)	$\nu/(\Omega D^2)$	$1 \cdot 10^{-12}$–$4 \cdot 10^{-11}$	10^{-5}–10^{-3}
Prandtl number (Pr)	ν/κ	10	1–10

determining the Rayleigh number from the total heat flow is discussed in Appendix B.

The Prandtl number in Table 1 is defined as the ratio of kinematic viscosity ν to thermal diffusivity κ, where both ν and κ are considered to be material constants. However, in a number of studies, including Soderlund (2019) and Amit et al. (2020), Pr is identified with the turbulent Prandtl number and its value is set to 1. This choice is usually justified by the fact that momentum transfer and heat transfer are not independent because they both depend on the same turbulent eddies (the principle known as the Reynolds analogy). In order to determine the sensitivity of the heat flux pattern to the Prandtl number, we consider three values: $Pr = 1$ (turbulent value), 3 and 10 (molecular value).

One of the goals of this paper is to estimate the latitudinal variations of the heat flux at the outer boundary of Titan's ocean. The heat flux variations can be characterized by two parameters (Amit et al., 2020). The first one is the latitudinal position of the heat flux maximum. Based on the position of this maximum, convection models can be subdivided into two end-member types — the equatorial cooling models where the heat transfer is maximum near the equator, and the polar cooling models where the maximum heat transfer occurs at high latitudes. The cooling pattern can be quantified by the ratio

$$q^{h/l} = \frac{\langle q \rangle^h - \langle q \rangle^l}{\langle q \rangle^h + \langle q \rangle^l}, \tag{1}$$

where $\langle q \rangle^h$ is the average heat flux at high latitudes ($\theta > \theta_{tc}$), $\langle q \rangle^l$ is the average heat flux at low latitudes ($\theta < \theta_{tc}$), and $\theta_{tc} = \arccos(r_i/r_o)$ (for more details, see Eqs. (11)–(13) in Amit et al. (2020)). The value of $q^{h/l}$ is positive for polar cooling and negative for equatorial cooling. The second parameter is the magnitude of the heat flux anomaly (Olson and Christensen, 2002), defined as the peak-to-peak amplitude of the zonally averaged heat flux, q^z, divided by twice the mean heat flux, $\bar{q}$,

$$q^* = \frac{q^z_{max} - q^z_{min}}{2\bar{q}}. \tag{2}$$

In order to answer the question of how the heat flux pattern depends on the thermal regime of the ocean, we need to know the criteria that separate the thermal regimes from each other. The transition to the non-rotating regime can be characterized by the convective Rossby number, Ro_c (Gilman, 1977), which is defined as the large scale ratio of the Coriolis force to the buoyancy force (Table 2). The convective Rossby number is a suitable measure for comparing weakly rotating systems but it fails as a diagnostic of the transition to the rapidly rotating regime which occurs at $Ro_c \ll 1$. According to King et al. (2010), this transition is controlled by the competition between the viscous and thermal boundary layers which occurs at $RaEk^{7/4} \approx 1$ (hereafter denoted by R_K, see Table 2). A similar condition ($RaEk^{12/7} \sim 1 - 100$, R_G in Table 2) was obtained by Gastine et al. (2016) who analyzed more than 200 models covering a broad parameter range with Ek and Ra spanning seven orders of magnitude (see also Eq. (24) in Julien et al. (2012b)). The parameter R_G may also serve as an alternative to the convective Rossby number. As demonstrated by Gastine et al. (2016, Fig. 16b), the Nusselt number (i.e., the total heat flow) is not affected by rotation when $R_G \gtrsim 100$. The last diagnostic parameter in Table 2 is the local convective Rossby number, which controls the breakdown of geostrophic balance in the thermal boundary layer (Julien et al., 2012a; Gastine et al., 2016).

3. Results of numerical simulations

We investigate thermal convection in a subsurface ocean using the Navier–Stokes–Boussinesq model. The basic equations and the numerical method are described in Appendix A. The computational domain is a spherical shell of inner radius r_i and outer radius r_o. The radius ratio r_i/r_o is set to 0.8 in all simulations. Convection is driven by a fixed temperature contrast between the inner and outer boundary and the gravity acceleration is proportional to r^{-2}. All models presented in this section have free-slip boundaries. The results obtained for models with no-slip boundary conditions are discussed in Section 4. The full list of the models explored in this study and the resulting values of Nu, Re (Reynolds number), q^* and $q^{h/l}$ are given in Tables C.4 and C.5 in Appendix C.

Fig. 1 shows the heat flux characteristics q^* and $q^{h/l}$ introduced in Section 2 as a function of diagnostic parameters Ro_c, Ro_{loc}, R_K and R_G. The results obtained for $Pr = 1$, 3 and 10 are plotted in blue, red and green, respectively. Inspection of the figure reveals that the time-averaged heat flux at the surface of the ocean strongly depends on the Prandtl number, which has been overlooked in previous studies (note that both Soderlund (2019) and Amit et al. (2020) use $Pr = 1$). The Prandtl number can influence not only the amplitude of the heat flux variations (panels a,c,e,g) but also the position of the global heat flux maximum (panels b,d,f,h). For example, for $R_K = 1$ (Fig. 1f), the model with $Pr = 10$ predicts enhanced polar cooling ($q^{h/l} \approx 0.4$) while the models with $Pr = 1$ and 3 predict equatorial cooling ($q^{h/l} \lesssim -0.4$).

Note that unlike the definitions of Ro_c and Ro_{loc}, where the Prandtl number appears in the denominator (Table 2), the definitions of R_K and R_G assume that the transition from the rapidly rotating to the non-rotating regime does not depend on the Prandtl number. Motivated by the fact that the buoyancy force in the momentum equation is scaled by Ra/Pr (see Eq. (A.1)), we introduce the modified dimensionless numbers R^*_K and R^*_G,

$$R^*_K = R_K/Pr, \quad R^*_G = R_G/Pr, \tag{3}$$

with the aim to minimize the scatter of the results. As shown in Fig. 2, the classification of the heat flux pattern in terms of R^*_K and R^*_G is independent of the value of Pr, meaning that all models with the same R^*_K or R^*_G show either polar cooling or equatorial cooling, depending on the sign of $q^{h/l}$. The graphs obtained for R^*_K and R^*_G are almost the same, which is not surprising given the similar definitions of R_K and R_G. In the following, we will use R^*_G which is based on simulations with $g \propto r^{-2}$ and $r_i/r_o = 0.6$ (Gastine et al., 2016), while R_K was numerically studied for an electrically conducting fluid, $g \propto r$ and $r_i/r_o = 0.35 - 0.4$ (King et al., 2010), i.e. for the parameters corresponding to the Earth's core rather than a subsurface ocean.

Inspection of Fig. 2b shows that the graph of $q^{h/l}$ intersects the horizontal axis at two points corresponding to a transition from equatorial to polar cooling (at $R^*_G \approx 1$) and from polar to equatorial cooling (at $R^*_G \approx 10$). The first transition represents a change from strong equatorial cooling at $R^*_G \lesssim 0.1$, where $q^{h/l} < -0.4$ and $q^* > 1$, to moderate to strong polar cooling at $R^*_G \gtrsim 1$, where $q^{h/l} = 0.1$–0.4 and $q^* = 0.3$–0.6. The transition is likely to be related to changes in the boundary layers, namely to the breakdown of the geostrophic turbulence followed by a regime of "unbalanced boundary layers" (Cheng et al., 2018). This interpretation is consistent with theoretical and experimental studies which show that this type of transition is described by the scaling law $Ra \propto Ek^{-1.80} - Ek^{-1.65}$ (Julien et al., 2012b; Ecke and Niemela, 2014).

The second transition (at $R^*_G \approx 10$) is less pronounced than the first one and is not accompanied by a significant change in q^*. As we will show later (Fig. 4), the heat flux pattern obtained for $R^*_G \approx 10$ has a

Table 2
Diagnostic parameters used in this study. The values in the third column are obtained using the scaling described in Appendix B. For a detailed discussion of different diagnostic parameters, see Soderlund (2019).

Parameter	Definition	Value on Titan	This study
Convective Rossby number (Ro_c)	$(RaEk^2/Pr)^{1/2}$	0.04–0.1	0.05–2.2
R_G	$RaEk^{12/7}$	40–100	0.5–150
R_K	$RaEk^{7/4}$	13–42	0.4–120
Local convective Rossby number (Ro_{loc})	$RaEk^{8/5}/Pr^{3/5}$	185–380	0.4–150

strong degree 4 zonal component and the transition does not represent a qualitative change in heat flux structure but rather a competition between the polar and equatorial maxima. The changes in the heat flux pattern are likely to be associated with the decreasing influence of rotation on a global scale and are not necessarily related to the processes in the boundary layers.

The values of R_G^* for which $q^{h/l} = 0$ are the same for different values of Ek and Pr, suggesting that the transitions between polar and equatorial cooling depend only on the diagnostic parameter R_G^* and do not depend on the specific choice of control parameters. Note that parameters Ro_c and Ro_{loc} predict the same transitions (Fig. 1b,d) but the position of the transition points depends on the Ekman number. For example, in the case of Ro_c (Fig. 1b), the transition from equatorial to polar cooling occurs at $Ro_c = 0.34$ for $Ek = 5 \cdot 10^{-4}$ (squares), at $Ro_c = 0.27$ for $Ek = 10^{-4}$ (circles) and at $Ro_c = 0.19$ for $Ek = 10^{-5}$ (triangles). We can see that the value of Ro_c at which the transition occurs decreases with decreasing Ek, suggesting that the transition value of Ro_c will be smaller than 0.1 for Ek relevant to Titan's ocean (Tables 1 and 2). An opposite trend is found for Ro_{loc} where the transition value increases as the Ekman number is decreased (compare the blue circles and triangles in Fig. 1d). This suggests that to characterize the transition from equatorial to polar cooling the diagnostic parameter must be proportional to $RaEk^{\alpha}$ where α is between 1.6 (corresponding to Ro_{loc}) and 2 (corresponding to Ro_c). These constraints are compatible with the theoretical ($\alpha = 1.67$) and experimental ($\alpha \in \langle 1.65, 1.80 \rangle$) results mentioned above and indicate that R_G^* ($\alpha = 1.71$) is a relevant parameter to assess the heat flux pattern in Titan's ocean.

While both Ro_c and Ro_{loc} fail to describe the first transition in a coherent way, the second transition can be equally well described by two conditions: $R_G^* = 10$ and $Ro_c = 1$ (see Fig. 1b). In Fig. 3, the transitions derived in this study are plotted in the parameter space with the x and y axis representing the influence of rotation (Ek) and the modified supercriticality of the Rayleigh number ($RaEk^{4/3}/Pr$), respectively (cf. Fig. 10 in Amit et al. (2020)). We can see that the values of the parameters relevant to Titan (indicated in red) lie between the lines $R_G^* = 1$ and $R_G^* = 10$ suggesting that Titan's ocean is in the polar cooling mode. This conclusion is consistent with the analysis based on the convective Rossby number, although as discussed above, this parameter is not suitable for the classification of the heat flux pattern as the lower bound of the interval in which the ocean is in the polar cooling mode depends on the Ekman number. Three black dashed lines in the middle of Fig. 3 show the lower bounds of Ro_c obtained for Ek between 10^{-5} and $5 \cdot 10^{-4}$. The dependence of the transitional value of Ro_c on Ek can be estimated by considering that $Ro_c = {R_G^*}^{1/2} Ek^{1/7}$ (see Table 2 and Eq. (3)). Since the transition from equatorial to polar cooling occurs at $R_G^* \approx 1$ and this condition is independent of the choice of Ek, the transitional value of Ro_c is approximately equal to $Ek^{1/7}$, implying that for realistic values of the Ekman number ($Ek < 10^{-10}$), the transitional value of the Rossby number is smaller than 0.04.

Fig. 4 shows the zonally averaged heat flux at the upper boundary of the ocean plotted as a function of the latitude. The curves are computed for three different values of Pr and different combinations of parameters Ra and Ek, corresponding to R_G^* between about 0.25 and 15. The heat transfer in the ocean is illustrated in Figs. 5 and 6 where we show the mean temperature and velocity fields for the models with $Pr = 1$ and 10, respectively. We will first discuss Figs. 4 and 5 and then compare Figs. 5 and 6.

The heat flux distribution obtained for $R_G^* < 0.5$ (Fig. 4a,b) is characterized by a strong degree 2 component and a pronounced equatorial cooling. The flow (Fig. 5a,b) is organized by the Coriolis force into narrow structures (Taylor columns) that are parallel to the rotation axis. The Reynolds stresses transfer the angular momentum of the cylindrical flow towards the equatorial region close to the outer boundary, giving rise to a prograde equatorial flow (Christensen, 2002) which tends to homogenize the temperature of the ocean near the equator (Guervilly and Cardin, 2017). The concentration of warm water outside the tangent cylinder (the cylinder of radius r_i whose axis is identical with the rotation axis) then leads to an efficient heat transfer at low latitudes. The cold region within the tangent cylinder is characterized by a stable thermal structure impeding the convective fluid motion (Olson et al., 1999).

As R_G^* increases, the magnitude of the heat flux in the equatorial region decreases, which is accompanied by an increase in heat transfer at high latitudes (Fig. 4c–e). During the transition from the equatorial to polar cooling, the models show a complex heat flux pattern, with pronounced peaks at mid-latitudes (Fig. 4d), implying a strong degree 6 component. The change in the heat flux pattern is a consequence of the increasing influence of inertial and buoyancy forces (Fig. 5c–e). The cylindrical flow structures gradually break down and the convective heat transfer at high latitudes starts to play a dominant role. The heat transfer inside the tangent cylinder at mid-latitudes is enhanced by the convective heating of waters near the surface while the prograde zonal flow inhibits the convective transfer of heat in the equatorial region (Yadav et al., 2016).

The maximum polar cooling is obtained when $R_G^* = 2-6$ (Fig. 4f,g). The columnar flow induced by the Coriolis force has disappeared and the Reynolds stress is too weak to drive the prograde zonal flow (Fig. 5f,g). Homogenization of angular momentum (Aurnou et al., 2007) leads to the reversal of the equatorial zonal flow from prograde (Fig. 5f) to retrograde (Fig. 5g) and the increase in the magnitude of zonal flow velocity inside the tangent cylinder. The mean vertical velocity in the equatorial region is close to zero. However, this finding should be interpreted with caution since turbulent heat transfer due to non-axisymmetric, instantaneous radial velocities may still be significant (Soderlund et al., 2013), as indicated by the local increase in heat flux near the equator. The efficiency of convective heat transfer increases at high latitudes where the effect of rotation on the flow is smaller than in the equatorial region (Guervilly and Cardin, 2017), though not negligible (note that the mean radial velocities still exhibit a significant amount of axial alignment).

The transition at $R_G^* = 10$ is accompanied by an increase of the heat transfer efficiency near the equator and a return to the equatorial cooling (Fig. 4h,i). The heat flux is dominated by zonal degree 2 and 4 terms, with peaks at the poles and the equator and two minima at mid-latitudes. The amplitude of the heat flux variations decreases and the pattern becomes less sensitive to changes in R_G^*. The equatorial region is characterized by strong retrograde flow and Hadley-like meridional circulation (Soderlund, 2019), with warm water rising near the equator and cold water sinking at "subtropical" latitudes (Fig. 5h,i). At $R_G^* \approx 16$, the flows inside the tangent cylinder have no preferred spatial orientation, indicating that the effect of rotation on the convection is negligible. When $R_G^* \gg 10$ the influence of rotation becomes negligible and the normalized heat flux is close to 1 (not shown here, but see Fig. 3a in Soderlund (2019)).

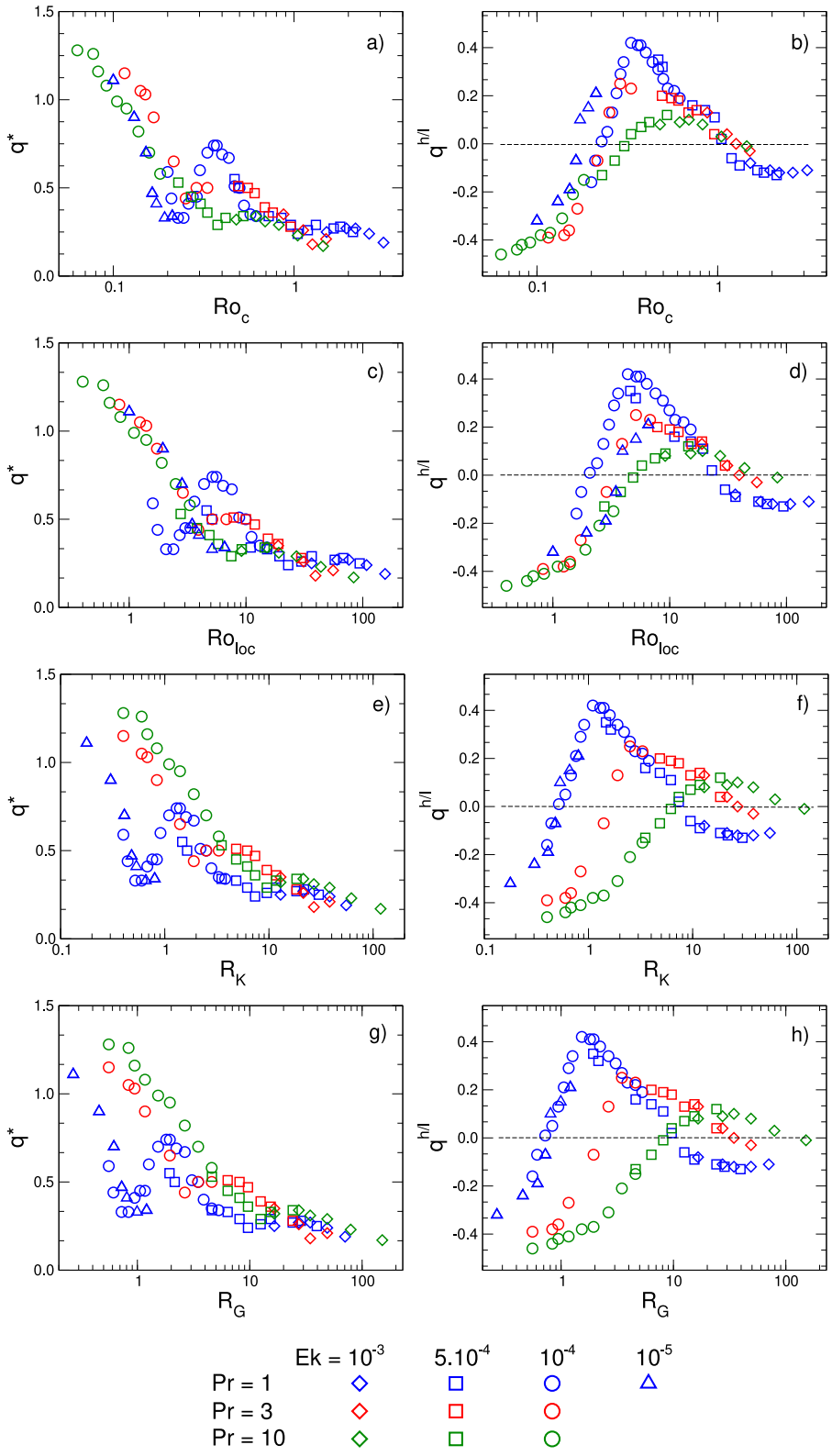

Fig. 1. Heat flux characteristics q^* and $q^{h/l}$ plotted as a function of different diagnostic parameters. The dashed lines mark the transition from equatorial ($q^{h/l} < 0$) to polar ($q^{h/l} > 0$) cooling. For the definition of parameters Ro_c, Ro_{loc}, R_K and R_G, see Table 2.

As discussed in connection with Figs. 1 and 2, the models with different Prandtl numbers give rather different values of q^*, especially for R_G^* between 1 and 10. Comparison of the curves in Fig. 4 shows that in most cases an increase in Pr causes a decrease in the amplitude of the heat flux peaks but only weakly affects the shape of the variations. The biggest difference is found for R_G^* between 1 and 3 where the models with $Pr = 10$ show a pronounced local maximum near the equator (Fig. 4d–f).

An increase in Pr generally leads to an enhancement of viscous forces and a reduction of turbulence (due to reduction of inertia forces).

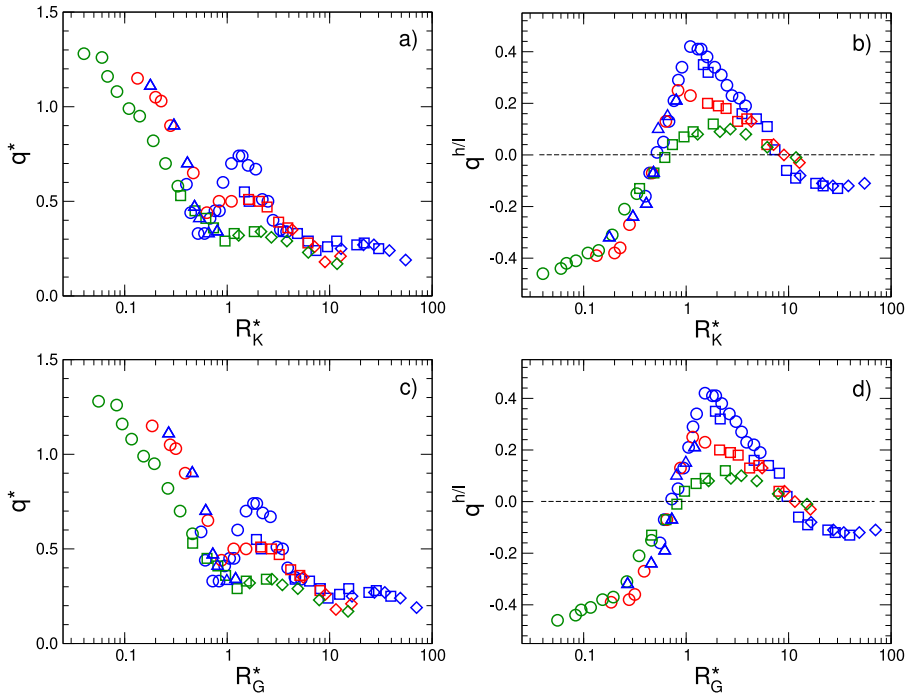

Fig. 2. Heat flux characteristics q^* and $q^{h/l}$ plotted as a function of modified diagnostic parameters $R_K^* = R_K/Pr$ and $R_G^* = R_G/Pr$. The symbols are the same as in Fig. 1. The dashed lines in panels b and d mark the transition from equatorial ($q^{h/l} < 0$) to polar ($q^{h/l} > 0$) cooling.

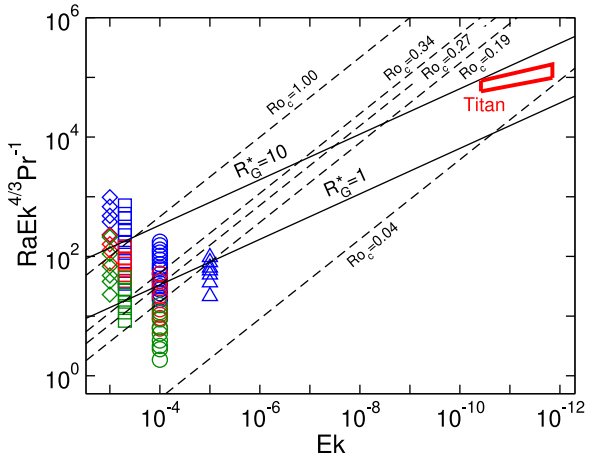

Fig. 3. Boundaries between the areas of polar and equatorial cooling plotted as a function of parameters Ek (decreasing from left to right) and $RaEk^{4/3}/Pr$. The boundaries are shown for two diagnostic parameters: the modified transition number R_G^* (preferred solution) and the convective Rossby number Ro_c. The parameters relevant to Titan's ocean (the red area in the graph on the right) lie between the lines $R_G^* = 1$ and $R_G^* = 10$ (full lines), suggesting that Titan's ocean is in the polar cooling mode ($q^{h/l} > 0$). The dashed lines show the transitions obtained from the analysis of the convective Rossby number. While the upper bound of the interval in which $q^{h/l} > 0$ is uniquely defined by $Ro_c = 1$, the lower bound decreases as the Ekman number is decreased. The three dashed lines in the middle of the figure correspond to (from left to right) $Ek = 5 \cdot 10^{-4}$, 10^{-4} and 10^{-5}. For the ocean to be in the polar cooling mode, Ro_c must be smaller than 0.04 when $Ek \lesssim 10^{-10}$. The symbols on the left side of the graph represent the numerical simulation (see Fig. 1 for the legend).

As a consequence, low Pr fluids produce more vigorous convection (higher Reynolds numbers), but lower heat transfer rates (lower Nusselt numbers) than moderate Pr fluids (for a review, see King and Aurnou (2013)). Inspection of Figs. 5 and 6 shows that the models with $Pr = 10$ follow the same trends as those with $Pr = 1$, but also reveals significant differences in the magnitude and spatial distribution of temperature and flow velocities. A full understanding of these differences would require a comprehensive analysis of the results which is beyond the scope of this study.

4. Role of boundary conditions

As mentioned in the introduction, Soderlund (2019) and Amit et al. (2020) differ in their conclusions regarding Titan's cooling pattern. While the former study suggests weak equatorial cooling, the results of the latter study are consistent with enhanced polar cooling. This discrepancy may be related to differences in boundary conditions: Unlike the study by Soderlund (2019), which investigates models with free-slip boundaries, the simulations by Amit et al. (2020) are performed with no-slip boundary conditions. It has been predicted that the thickness of the Ekman layer goes to zero for low Ekman numbers (Zhang and Jones, 1993), implying that the free-slip and no-slip models should give similar heat flux patterns for realistic values of Ek ($\sim 10^{-12} - 10^{-11}$). However, such values can hardly be reached by the present-day numerical simulations because of insufficient computing power. Although no-slip is the proper boundary condition for a viscous fluid at a rigid boundary, computationally feasible no-slip models may overestimate viscous effects (Kuang and Bloxham, 1997), resulting in a heat flux pattern that is different from that obtained for models with free-slip boundaries.

In Fig. 7, we compare the results obtained for models with no-slip (black) and free-slip (blue) boundary conditions. The models are computed for $Pr = 1$, i.e. the same as in the studies by Soderlund (2019) and Amit et al. (2020). The heat flux characteristics q^* and $q^{h/l}$ are plotted as a function of the parameter R_G^* but the same conclusions can be drawn for the convective Rossby number, Ro_c. Inspection of the figure shows that the two types of models give similar results for $R_G^* \lesssim 0.7$, but they predict significantly different heat flux characteristics for $R_G^* > 1$. While the no-slip models show the transition from equatorial to polar cooling with increasing R_G^*, the free-slip models show a more complex trend, suggesting the existence of a distinct cooling pattern in the transitional regime ($1 < R_G^* < 10$) manifested by an increase in heat flux at $R_G^* \approx 2$.

Fig. 8 shows the zonally averaged heat flux at the upper boundary of the ocean plotted as a function of the latitude for six different values

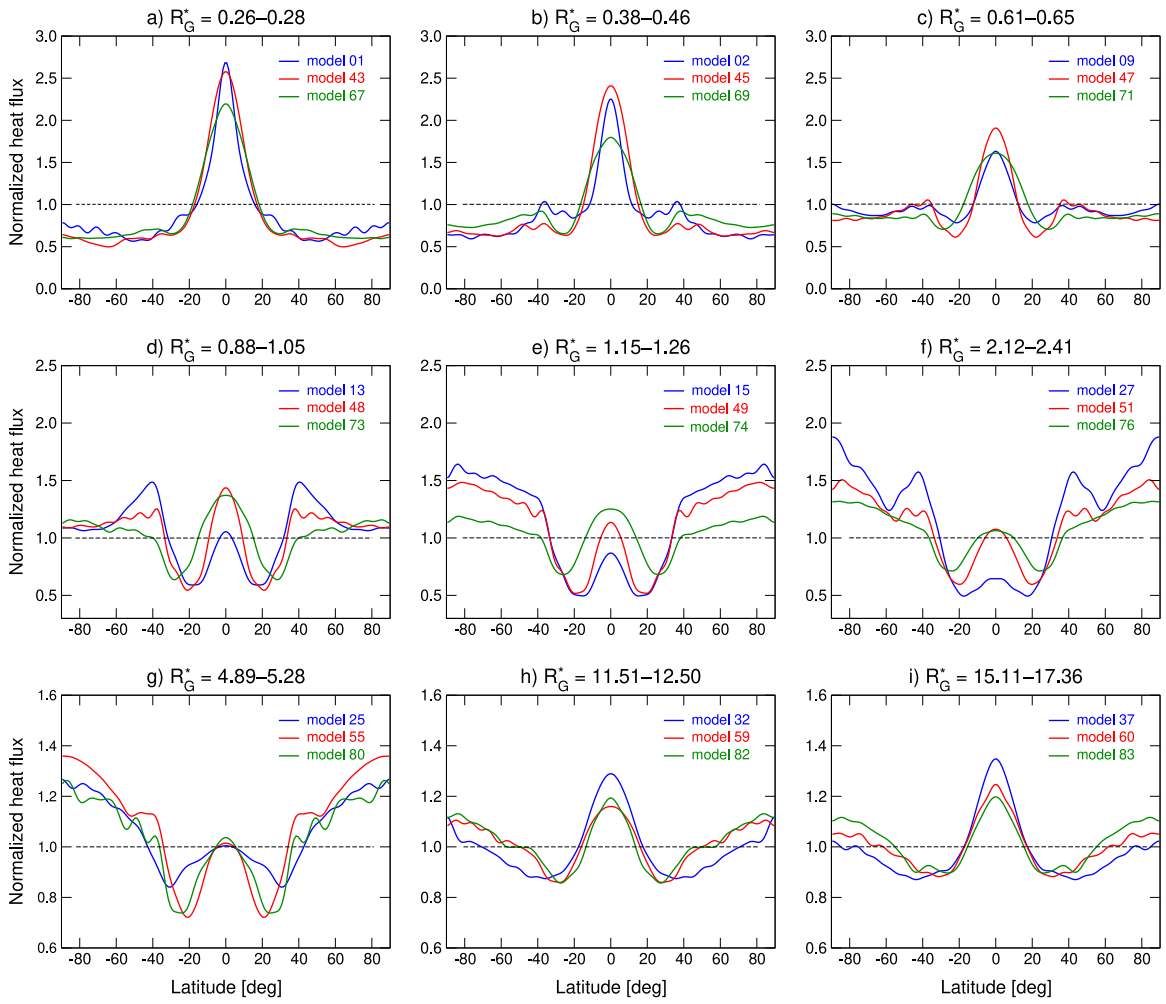

Fig. 4. Time and zonally averaged heat flux at the upper boundary of the ocean plotted as a function of the latitude for different values of R_G^*. The blue, red and green curves correspond to $Pr = 1$, 3 and 10, respectively. The heat flux is normalized such that the total heat flux is 1. The values of parameters Ra and Ek corresponding to the individual curves can be found in Table C.5. Note that the plots have different vertical scales. Time averaging is performed over at least 0.02 viscous diffusion times. (For interpretation of the references to color in this figure legend, the reader is referred to the web version of this article.)

of R_G^*. The heat flux in models with small R_G^* (Fig. 8a) is characterized by a strong degree 2 component and a pronounced equatorial cooling. As R_G^* increases, the magnitude of the heat flux in the equatorial region decreases, which is accompanied by an increase in convective heat transfer at high latitudes (Fig. 8b). During the transition from the equatorial to polar cooling, the no-slip models retain some resemblance to the fast-rotating models (note the broad heat flux maximum at the equator), in contrast to the free-slip models which show a more complex heat flux pattern, with two pronounced peaks at mid-latitudes. The polar cooling reaches a maximum at $R_G^* \approx 2$ for both the free-slip and no-slip models (Fig. 8c,d). However, while the heat flux curve obtained for the free-slip boundary condition shows a significant decrease near the equator and two pronounced maxima at the poles, and therefore corresponds to the spherical harmonics Y_{20}, the heat flux in the no-slip model is dominated by a degree 4 pattern, with a local maximum at the equator and two minima at mid-latitudes. As R_G^* further increases (Fig. 8e), the polar cooling becomes less efficient. In the case of the no-slip boundary condition, the shape of the heat flux curve remains the same as in the polar cooling mode shown in Fig. 8d, but the amplitude of the heat flux variations decreases. In contrast, the decrease of polar amplitudes in the free-slip models is accompanied by an increase of the heat transfer efficiency near the equator and a return to the equatorial cooling (Fig. 8f).

Our results suggest that the discrepancy between the conclusions of Soderlund (2019) and Amit et al. (2020) is related to the different boundary conditions. Based on the numerical simulations with free-slip boundary conditions corresponding to R_G^* between 2.5 and 490, Soderlund (2019) predicts the transition from equatorial to polar cooling with increasing influence of rotation (i.e. with decreasing R_G^*, see Fig. 3 therein). This is in good agreement with the results obtained in our study and shown in panels d–h of Fig. 8 (note that R_G^* in Fig. 3 in Soderlund (2019) decreases from left to right). However, Soderlund (2019) fails to identify the transition from polar to equatorial cooling which occurs at $R_G^* \approx 1$, because this value is outside the range of tested parameters. The existence of this transition was demonstrated by Amit et al. (2020) who performed numerical simulations with no-slip boundary conditions for R_G^* ranging from 0.4 to 45 (see Fig. 7 therein). Our results confirm the general trend predicted for no-slip models by Amit et al. (2020), namely the transition from equatorial to polar cooling with increasing R_G^*, but give slightly different heat flux curves. This discrepancy may be related to the different lateral resolutions of the models or to the differences in gravitational acceleration ($g \propto r$ in Amit et al. (2020) while $g \propto r^{-2}$ in the present study).

5. Comparison with Titan's topography

Fig. 9 shows two end-member models of how the heat flux from the ocean can influence the shape of the ice shell. The first model (Fig. 9a) assumes that the ice shell is rigid and the heat is transferred by conduction. A higher-than-average heat flux from the ocean causes the

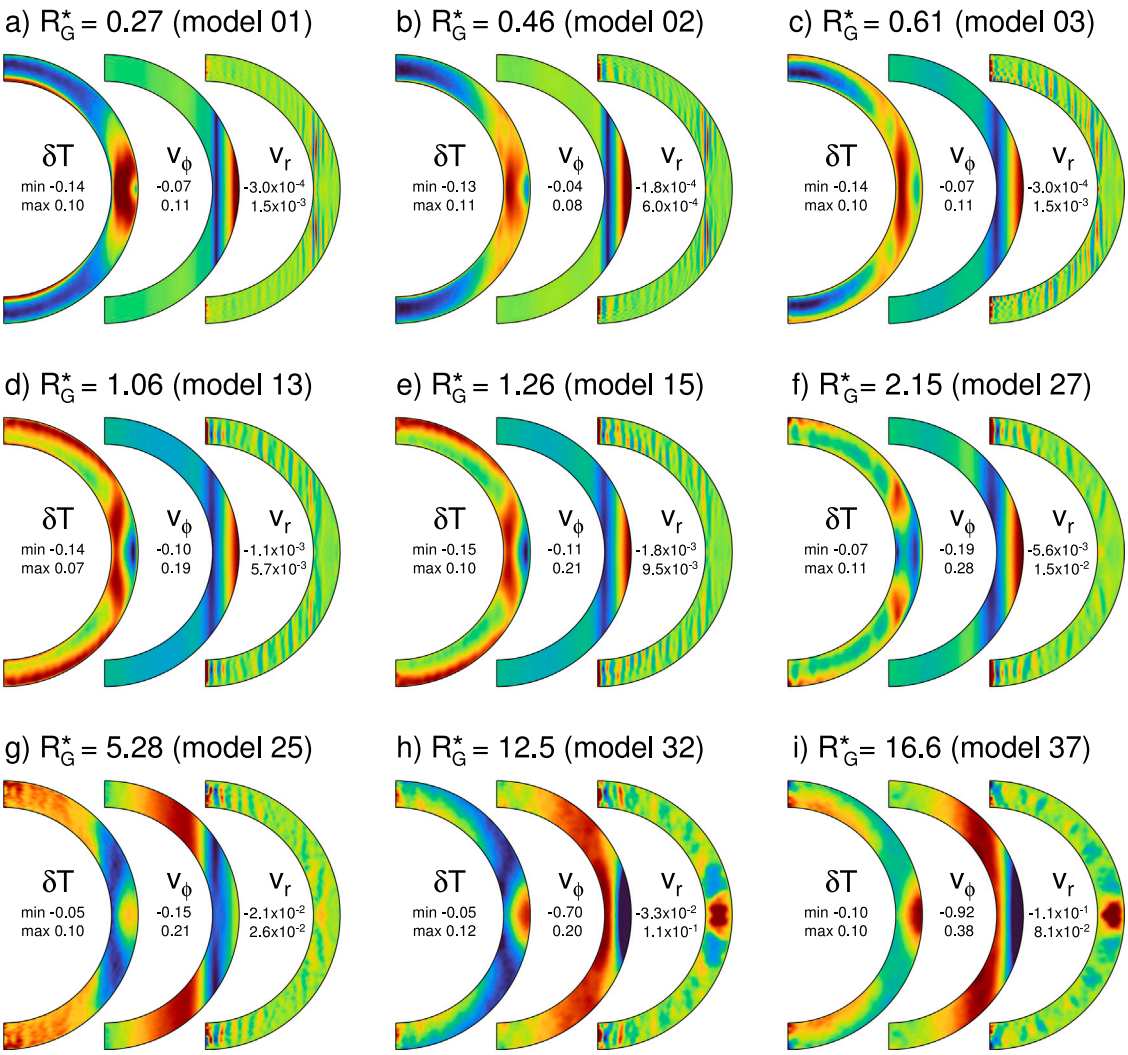

Fig. 5. Temperature and velocity fields averaged over time and longitude. All models are computed for $Pr = 1$ and correspond to those shown in Fig. 4 (blue lines). Symbol δT denotes the dimensionless temperature variations taken relative to the average temperature profile while v_ϕ and v_r are the azimuthal and radial components of the flow velocity, respectively, given in Rossby number units, $U/(\Omega D)$, where U is the mean velocity in the ocean. The minimum and maximum values of δT, v_ϕ and v_r are given on the left-hand side of each cross section. Red (blue) denotes positive (negative) values. (For interpretation of the references to color in this figure legend, the reader is referred to the web version of this article.)

melting of ice and subsequent thinning of the ice shell. The decrease in pressure along the ice–water boundary is then compensated by negative surface topography, in agreement with the Airy compensation model (Kvorka et al., 2018; Čadek et al., 2019a).

The convection scenario (Fig. 9b) has not yet been investigated in detail, but its potential importance has been recognized recently in several studies of early magma oceans (e.g. Labrosse et al., 2018; Morison et al., 2019; Agrusta et al., 2020). The convecting ice shell is on average warmer and less viscous than in the conductive case, which causes that the molten ice in the region of the enhanced heat flux is continuously replenished by the low viscosity ice flowing from the interior of the ice shell. The shape of the bottom boundary remains unchanged and since the temperature of ice above the region of the enhanced heat flux is on average higher than elsewhere, the model is characterized by elevated topography, in agreement with the Pratt compensation model. The same heat flux anomaly can therefore produce either positive or negative topography, depending on which mode of heat transfer is dominant. The question of whether Titan's ice shell is presently convecting or whether heat is transferred only by conduction is difficult to answer because the parameters controlling the onset of convection (grain size, thickness of the ice shell, temperature of the ocean, etc.) are not known with sufficient accuracy. In this section, we address this issue by comparing the results of our numerical simulations with Titan's long-wavelength topography.

The map of Titan's topography referenced to the geoid and expanded to spherical harmonic degree and order 5 is shown in Fig. 10a. The topography is characterized by depressions near the poles and several elevated areas at mid-latitudes. A significant portion (53%, measured by the L^2-norm) of the topographic signal is produced by zonal degree 2 and degree 4 terms (Fig. 10b). The topography is highly compensated (Durante et al., 2019) and is not significantly affected by tidal heating in the ice shell (Čadek et al., 2021).

The results presented in Section 3 suggest that the heat flux from Titan's ocean is maximum at the poles and its pattern is dominated by the same harmonic components as the topography ($\ell = 2$ and 4, $m = 0$, see Fig. 10c). Comparison of panels b and c of Fig. 10 reveals a high degree of similarity between some of the heat flux models derived in this study and the equatorially symmetric part of Titan's topography, thus supporting the hypothesis that the heat transfer in Titan's ice shell occurs by conduction and the latitudinal variations in topography are caused by uneven heating at the ice–water boundary. The correlation between the topography and the heat flux is excellent for all models with $Pr = 10$ (plotted in green) and also for models 25 ($Pr = 1$) and 56 ($Pr = 3$). Note that models 25 and 79 are almost identical.

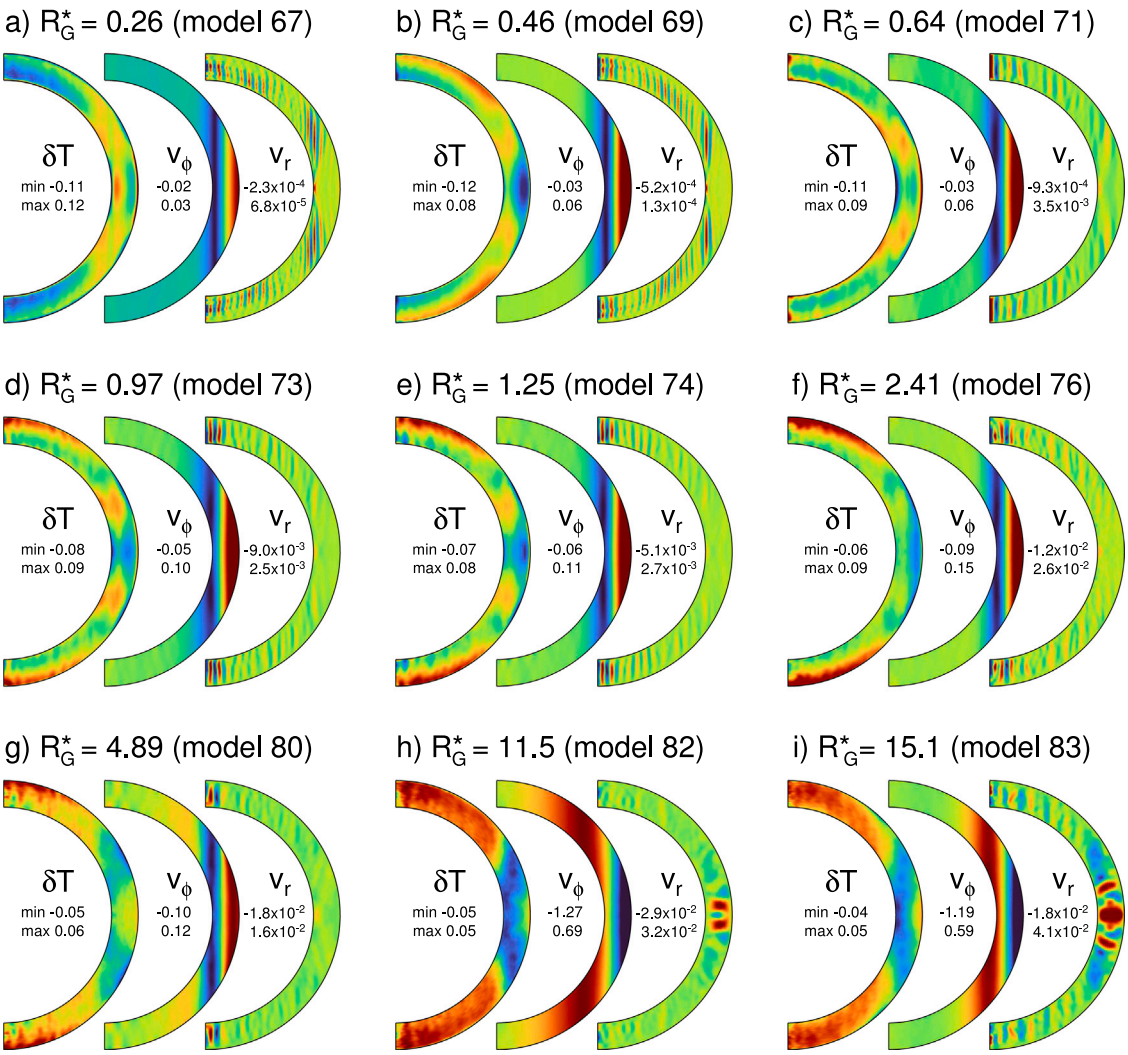

Fig. 6. As in Fig. 5 but for $Pr = 10$.

The magnitude of heat flux induced topography depends on the amplitude and wavelength of the heat flux variations and the viscosity of ice at the base of the ice shell, which in turn depends on the temperature of the ocean and the grain size of ice (see Fig. 5 in Kvorka et al. (2018)). The total heat production of Titan is estimated to be between 250 and 545 GW (Kalousová and Sotin, 2020), corresponding to an average heat flux of $3.2 - 6.9\,\mathrm{mW/m^2}$. The amplitude of the heat flux variations can be determined from Fig. 2. Taking into account that $R_G^* = 3{-}10$ on Titan (Table B.3), we get $q^* = 0.25{-}0.5$, which multiplied by the average heat flux results in an amplitude of $0.8{-}3.4\,\mathrm{mW/m^2}$. For simplicity, we will assume that the thickness of the ice shell is 100 km and the temperature of the ocean is 262 K (i.e., equal to the melting temperature of pure water ice). As shown by Kvorka et al. (2018), the topographic lows ($\lesssim -300$ m) observed in Titan's polar regions can be explained by a conductive ice shell model with 10 mm grain size and a heat flux amplitude of $1\,\mathrm{mW/m^2}$, or 3 mm grain size and a heat flux amplitude of $3\,\mathrm{mW/m^2}$. These values are well within the range of grain sizes expected on icy moons (Barr and McKinnon, 2007) and are likely compatible with the assumption of conduction dominated heat transfer (Běhounková et al., 2013).

Although our model provides a plausible explanation of degree 2 and 4 zonal topography, it cannot account for the longitude dependent part of the topographic signal or the fact that the topography is more pronounced in the southern than in the northern hemisphere. It is therefore likely that other effects, such as ethane precipitation (Choukroun and Sotin, 2012), climatically controlled erosion (e.g. Moore and Pappalardo, 2011) or convection in Titan's high pressure ice layer (Choblet et al., 2017a), can also contribute to the development of the long-wavelength topography, or that some of the topographic features are of ancient origin.

Our results provide indirect evidence that the heat in Titan's ice shell is transferred by conduction. However, it cannot be excluded that the ice shell is vigorously convecting and the heat flux from the ocean has little to no effect on the topography. If this is the case then it is likely that Titan's surface is shaped by external processes, such as aeolian and fluvial erosion, methane and ethane precipitation, etc., and internal processes associated with lateral variations in ice properties, such as porosity or presence of methane clathrate (Čadek et al., 2021).

6. Conclusions

The evolution of Titan's ice shell is primarily controlled by the heat transferred from the core to the surface. The heat produced in the deep interior is redistributed by ocean circulation, which is modulated by the Coriolis force, resulting in a latitudinal gradient in heat flux at the base of the ice shell. The recent studies by Soderlund (2019) and Amit et al. (2020) agree that the time-averaged heat flux can vary by tens of percent, but they differ in the predicted distribution of heat flux anomalies. In the present study, we show that this difference is related to the different boundary conditions used in the simulations. Although

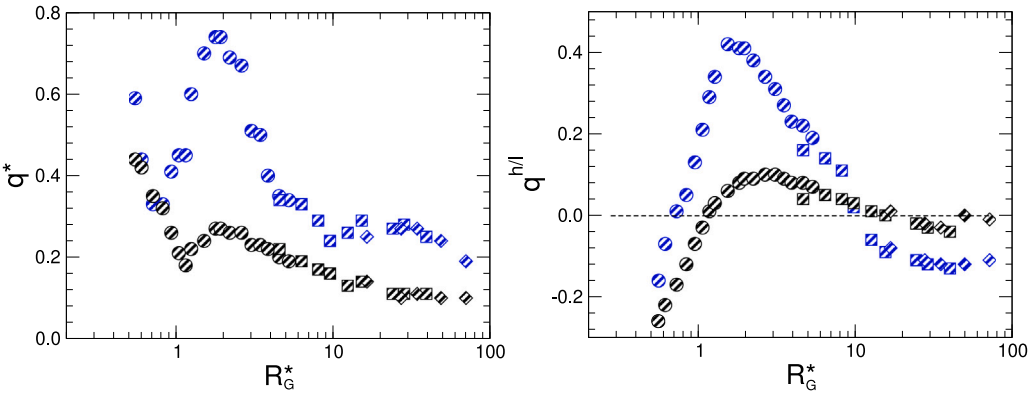

Fig. 7. Heat flux characteristics q^* and $q^{h/l}$ as a function of the convective Rossby number computed for models with no-slip (black) and free-slip (blue) boundary conditions. The Prandtl number is set to 1 in all simulations. Circles, squares and diamonds correspond to $Ek = 10^{-4}$, $5 \cdot 10^{-4}$ and 10^{-3}, respectively. (For interpretation of the references to color in this figure legend, the reader is referred to the web version of this article.)

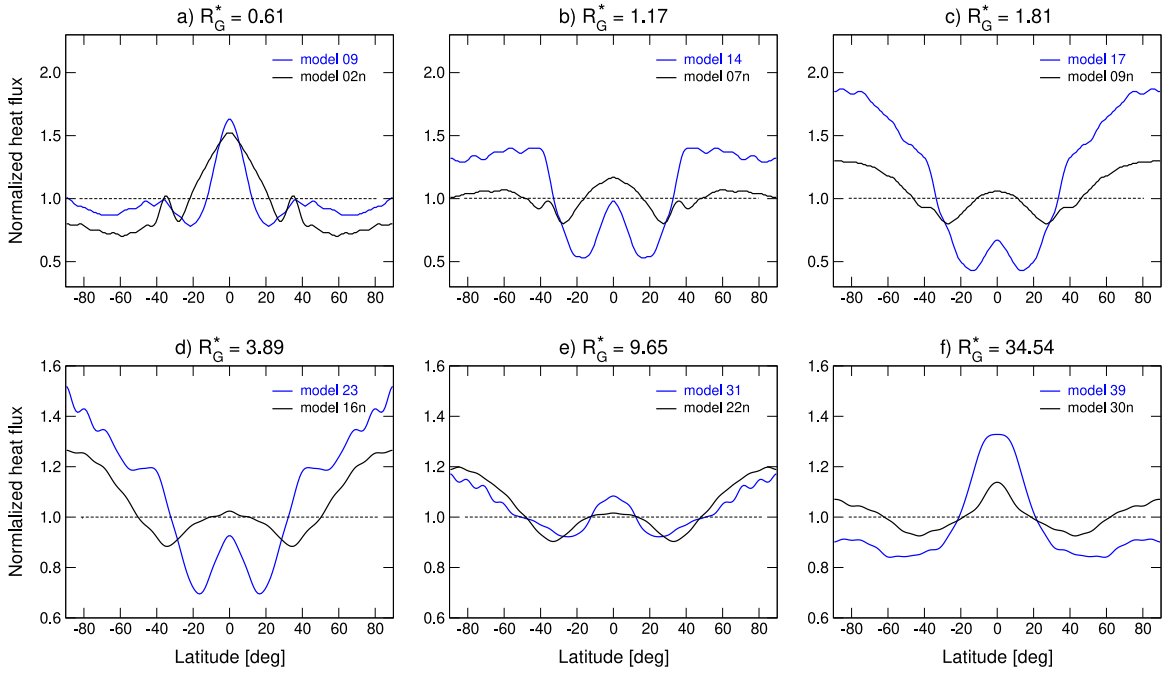

Fig. 8. Time and zonally averaged heat flux at the upper boundary of the ocean plotted as a function of the latitude. The blue and black curves correspond to models with free-slip and no-slip boundary conditions, respectively. The models are computed for $Pr = 1$ and different values of the parameter R^*_G, Eq. (3). The values of parameters Ra and Ek corresponding to the individual curves can be found in Tables C.4 and C.5. (For interpretation of the references to color in this figure legend, the reader is referred to the web version of this article.)

the models with free-slip and no-slip boundary conditions are expected to give similar results for $Ek \to 0$, they can predict different heat flux patterns for control parameters that are accessible with current computer power. Since the Ekman number used in numerical simulations is many orders of magnitude larger than in the real ocean, the no-slip models tend to overestimate viscous effects and, therefore, their results should be interpreted with caution.

One of the limitations of previous studies was that they did not investigate the dependence of the heat flux distribution on the Prandtl number. We show that even small changes in the Prandtl number can have a large impact on the magnitude of the heat flux anomaly. The effect of the Prandtl number is especially pronounced in the transitional regime where models with $Pr = 1$ show significantly stronger polar cooling than those with $Pr = 10$.

In order to determine the heat flux distribution at the upper boundary of Titan's ocean, we constructed a set of about 80 ocean models, varying all relevant control parameters (Ra, Ek, Pr) by at least one order of magnitude. The heat flux characteristics of the models were interpreted in terms of the modified transitional number $R^*_G = RaEk^{12/7}Pr^{-1}$. Depending on the relative importance of rotation, the heat flux from the ocean is concentrated either near the equator (equatorial cooling) or at high latitudes (polar cooling). Our analysis suggests that equatorial cooling occurs when $R^*_G < 1$ or $R^*_G > 10$ while polar cooling occurs when $R^*_G \in \langle 1, 10 \rangle$. Based on this result, we predict that the heat flux on Titan peaks near the poles and is dominated by zonal degree 2 and 4 terms. The predicted heat flux distribution is negatively correlated with the axisymmetric part of Titan's long-wavelength topography, suggesting a coupling between ocean dynamics and the evolution of the ice shell (Kvorka et al., 2018). It is likely that variations in the heat flux from the ocean also influence the evolution of other icy moons (e.g. Soderlund et al., 2014; Čadek et al., 2019b).

The approach developed in this work is applicable to icy moons where the ocean is underlain by a layer of high-pressure ice, which guarantees that the temperature at the bottom boundary of the ocean is constant. This is clearly not the case of Enceladus where the ocean circulation may be affected by uneven tidal heating in its porous

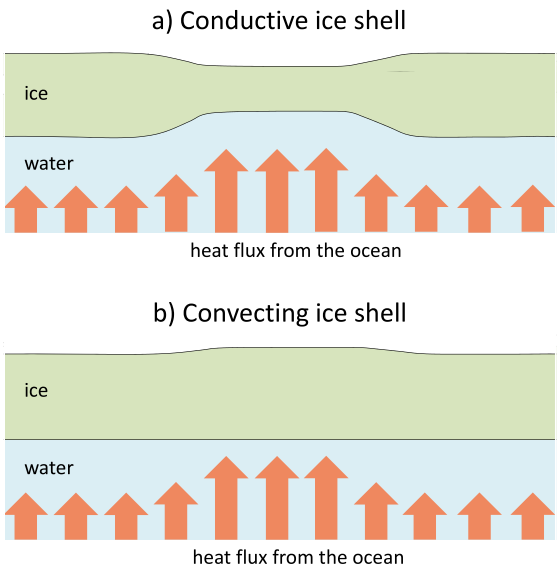

Fig. 9. The response of the ice shell to variations in ocean heat flux is controlled by the viscosity of ice. (a) If the ice shell is rigid and transfers the heat by conduction, lateral variations in heat flux cause thinning of the shell in regions of high heat flux and thickening of the shell in regions of low heat flux (Kvorka et al., 2018). (b) If the viscosity of ice near the base of the ice shell is low and heat transfer occurs by convection, the shape of the bottom boundary remains essentially unchanged. The surface topography is smaller than in the conduction case and has the opposite sign (Kihoulou et al., 2021). We assume that in both cases the surface temperature is constant, in accordance with the conditions prevailing on Titan.

core (Choblet et al., 2017b), or Europa where the temperature of the oceanic floor may vary due to magmatic processes in the silicate mantle (Běhounková et al., 2021). Throughout the paper, we neglect the effect of salinity variations on the density of ocean water. As recently shown by Zeng and Jansen (2021), this effect may be important but it is difficult to implement due to the lack of knowledge about the composition of Titan's ocean. In the case of polar cooling, the presence of freshwater lenses due to melting in the polar regions could lead to further increase in heat flux at high latitudes (Lobo et al., 2021).

Acknowledgments

The authors thank two anonymous reviewers for their critical reviews and constructive suggestions and Martin Kihoulou for valuable discussions.

Appendix A. Governing equation and numerical method

The models discussed in this paper have been obtained by simultaneously solving the Navier–Stokes equation including the Coriolis force, the transport equation for temperature and the mass conservation equation for an incompressible fluid. The variables in the equations are non-dimensionalized using the following scaling parameters: the thickness of the ocean, $D = r_o - r_i$, the superadiabatic temperature contrast, ΔT, and the viscous diffusion time, $\tau = D^2/\nu$, where ν is the kinematic viscosity. The governing equations then take the form (cf. Gastine et al., 2016):

$$-\nabla p' + \nabla^2 \boldsymbol{v}' - \frac{Ra}{Pr} T' f(r) \boldsymbol{e}_r - \frac{2}{Ek} \boldsymbol{e}_z \times \boldsymbol{v}' = \frac{\partial \boldsymbol{v}'}{\partial t'} + \boldsymbol{v}' \cdot \nabla \boldsymbol{v}', \tag{A.1}$$

$$\frac{\partial T'}{\partial t'} = \frac{1}{Pr} \nabla^2 T' - \boldsymbol{v}' \cdot \nabla T', \tag{A.2}$$

$$\nabla \cdot \boldsymbol{v}' = 0. \tag{A.3}$$

Here, $t' = t/\tau$ is the dimensionless time, $\boldsymbol{v}' = \boldsymbol{v}(\tau/D)$ is the dimensionless velocity, $T' = (T - T_o)/\Delta T$ is the dimensionless temperature (with T_o the temperature at the outer boundary), $p' = p(\tau\rho/\nu)$ is the dimensionless pressure (with ρ the density), $f(r) = r_o^2/r^2$ is the function describing the radial variations of the gravitational acceleration, $\boldsymbol{e}_r$ is the radial unit vector, $\boldsymbol{e}_z$ is the unit vector parallel to the angular velocity vector, and Ra, Ek and Pr are the control parameters defined in Table 1. Note that Ek in Table 1 is a factor of two larger than that used in Soderlund (2019).

The dimensionless temperature, T', is fixed to 1 on the inner boundary and to 0 on the outer boundary. Two types of mechanical boundary conditions are considered: no-slip,

$$\boldsymbol{v}' = \boldsymbol{0}, \tag{A.4}$$

and free-slip,

$$\boldsymbol{v}' \cdot \boldsymbol{e}_r = 0, \quad \boldsymbol{\sigma}' \cdot \boldsymbol{e}_r - (\boldsymbol{e}_r \cdot \boldsymbol{\sigma}' \cdot \boldsymbol{e}_r)\boldsymbol{e}_r = \boldsymbol{0}, \tag{A.5}$$

where $\boldsymbol{\sigma}'$ is the dimensionless stress.

Eqs. (A.1)–(A.3) are reformulated as a system of first order partial differential equations (i.e., in terms of variables $\boldsymbol{v}'$, $\boldsymbol{\sigma}'$, T' and $\nabla T'$) and solved using a pseudo-spectral method based on spherical harmonic expansions in angular coordinates and finite differences in radius. The expansions are truncated at degree $\ell_{max} = 120 - 215$ and the spherical harmonic coefficients are discretized in 65–97 unevenly spaced Chebyshev points in radius. At each time step, the nonlinear terms are evaluated on an auxiliary grid consisting of $3\ell_{max}/2+1$ Gauss–Legendre points in latitude and $3\ell_{max} + 1$ equally spaced points in longitude, and transformed back to the spectral domain using the Gauss–Legendre integration method and the fast Fourier transform (Martinec, 1989). The time derivatives are discretized using a hybrid approach in which the Crank–Nicolson method is applied to the diffusion terms and an explicit second order Adams–Bashforth method is applied to the nonlinear terms and the Coriolis force. The method described above has been implemented in the Fortran language and tested against the results of Gastine et al. (2016).

Appendix B. Control parameters relevant to Titan's ocean

The evaluation of Pr and Ek is straightforward because the molecular values of ν and κ for water are known and the thickness of the ocean (D) can be estimated from geophysical observations (Table B.3). The evaluation of the Rayleigh number,

$$Ra = \frac{\alpha g_o \Delta T D^3}{\kappa \nu}, \tag{B.1}$$

requires the knowledge of the adiabatic temperature contrast across the ocean (ΔT). An estimate of ΔT can be derived using the relationship between the Rayleigh number and the Nusselt number (Nu), whose value can be determined from the heat output of the icy satellite. Using the scaling laws for two end-members, corresponding to the rapidly rotating (RR) and non-rotating (NR) heat transfer regimes, Soderlund (2019) obtained

$$\Delta T_{NR} = 7.3 \left(\frac{\nu}{\alpha g_o \rho C_p} \right)^{1/4} \bar{q}^{3/4}, \tag{B.2}$$

$$\Delta T_{RR} = 2.1 \left(\frac{\Omega^4 \kappa}{\rho^2 C_p^2 \nu \alpha^3 g_o^3} \right)^{1/5} (\bar{q}^2 D)^{1/5}, \tag{B.3}$$

where $\bar{q}$ is the average heat flux. Eqs. (B.2) and (B.3) follow from the relationships $Nu = 0.07 Ra^{1/3}$ (Gastine et al., 2015) and $Nu = 0.15 Ra^{3/2} Ek^2$ (Gastine et al., 2016), respectively. The total heat production of Titan and the parameters of its ocean are not fully known (e.g. Vance et al., 2018). In this paper, we assume that $D \in \langle 100, 500 \rangle$ km, $\bar{q} \in \langle 3, 7 \rangle$ mW/m^2 (Kalousová and Sotin, 2020), $\rho = 1200$ kg m^{-3}, $g_0 = 1.4$ m s^{-2}, $\alpha = 3.2 \cdot 10^{-4}$ K^{-1}, $C_p = 2800$ J kg^{-1}K^{-1} and diffusivities ν and κ represent material parameters ($\nu = 1.8 \cdot 10^{-6}$ m^2/s, $\kappa = 1.8 \cdot 10^{-7}$

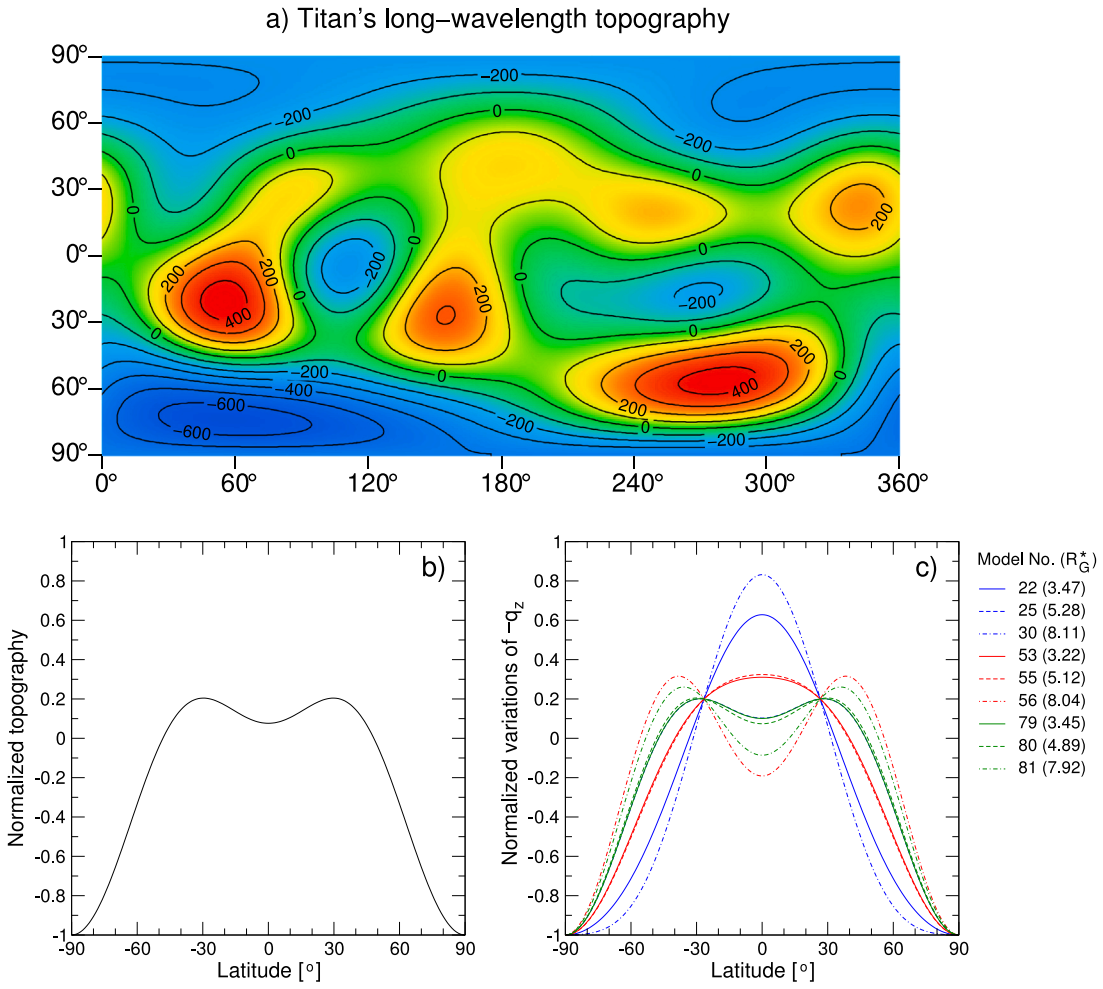

Fig. 10. (a) Topography of Titan (i.e., the height measured from the geoid) expanded to spherical harmonic degree and order 5. Topography is computed using the shape model by Corlies et al. (2017), gravity model by Durante et al. (2019) and the standard formula for the static tidal and centrifugal potentials. The contour interval is 100 m. (b) Equatorially symmetric and zonally averaged topography of Titan as a function of latitude. (c) Latitudinal variations in the heat flux computed for free-slip models with R_G^* ranging between 3 and 10 (cf. Table B.3). The models with $Pr = 1$, 3 and 10 are plotted in blue, red and green, respectively. As in the case of panel b, we only plot the equatorially symmetric part of the field ($C_{20}Y_{20}+C_{40}Y_{40}$). To facilitate the comparison, topography and heat flux are normalized to 1 and q^z is plotted with the opposite sign. (For interpretation of the references to color in this figure legend, the reader is referred to the web version of this article.)

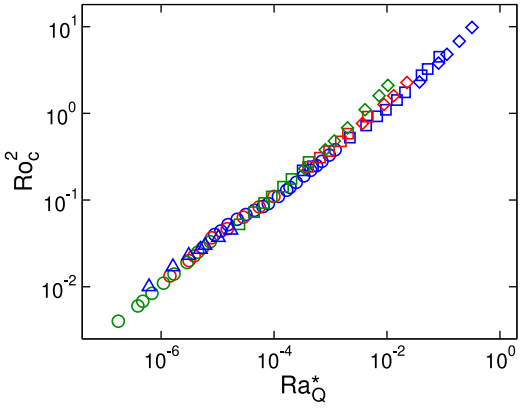

Fig. B.11. Square of the convective Rossby number as a function of the modified Rayleigh number. The data plotted in the figure can be found in Table C.5.

m^2/s). Substituting these values into Eqs. (B.1)–(B.2) then gives $Ra \in \langle 2.5 \cdot 10^{19}, 10^{23} \rangle$.

An alternative estimate of Ra can be obtained using the 'diffusivity-free' scaling proposed for free-slip models by Christensen (2002) and elaborated by Aubert (2005) and Christensen and Aubert (2006). Assuming that the diffusivities play a minor role in global heat transfer, Christensen and Aubert (2006) introduced a new type of the Nusselt number that characterizes the advected heat flow:

$$Nu^* = \frac{1}{4\pi r_o r_i} \frac{Q_{adv}}{\rho C_p \Omega D \Delta T} = (Nu - 1) Ek/Pr\,, \tag{B.4}$$

where r_o and r_i are the outer and inner radii of the ocean, Q_{adv} is the advected heat flow, i.e. the total heat flow Q corrected for the conductive heat flow Q_{cond}, and Nu is the Nusselt number defined as

$$Nu = \frac{Q}{Q_{cond}} = \frac{1}{4\pi r_o r_i} \frac{QD}{\rho C_p \kappa \Delta T}\,. \tag{B.5}$$

Note that definition (B.5) is slightly different from the definition used by Soderlund (2019) and Amit et al. (2020), which does not include the correction for sphericity. Similarly, one can define a modified Rayleigh number that depends on Q_{adv} and does not depend explicitly on ΔT:

$$Ra_Q^* = \frac{1}{4\pi r_o r_i} \frac{\alpha g_o Q_{adv}}{\rho C_p \Omega^3 D^2} = Ra(Nu - 1) Ek^3/Pr^2\,. \tag{B.6}$$

Using an extensive set of simulations, Christensen and Aubert (2006) showed that the relationship between Nu^* and Ra_Q^* can be approximated by a simple power-law expression, valid for a broad range of parameters:

$$Nu^* = c\, Ra_Q^{*\,\gamma}\,, \tag{B.7}$$

Table B.3
Values of control and diagnostic parameters expected for different thicknesses of Titan's ocean. The modified Rayleigh number, Ra_Q^*, and the Rayleigh number, Ra, are obtained from Eqs. (B.6) and (B.9), respectively, where $Q_{adv} = 250-545$ GW (Kalousová and Sotin, 2020), $r_o = 2500$ km and $r_i = r_o - D$. The remaining parameters are calculated using the definitions given in Tables Tables 1 and 2 and Eq. (3).

Parameter	Realistic range				
D [km]	100	200	300	400	500
Ra_Q^*	$(4.5–9.9)\cdot10^{-7}$	$(1.2–2.6)\cdot10^{-7}$	$(0.6–1.2)\cdot10^{-7}$	$(3.2–7.1)\cdot10^{-8}$	$(2.2–4.8)\cdot10^{-8}$
Ek	$3.9\cdot10^{-11}$	$9.8\cdot10^{-12}$	$4.3\cdot10^{-12}$	$2.4\cdot10^{-12}$	$1.6\cdot10^{-12}$
Ra	$(4.5–6.8)\cdot10^{19}$	$(3.5–5.4)\cdot10^{20}$	$(1.2–1.8)\cdot10^{21}$	$(2.9–4.4)\cdot10^{21}$	$(5.7–8.6)\cdot10^{21}$
Ro_{loc}	252–379	217–326	200–302	191–288	185–279
Ro_c	0.08–0.10	0.06–0.07	0.05–0.06	0.04–0.05	0.04–0.05
R_G^*	6.5–9.8	4.8–7.2	4.0–6.0	3.6–5.4	3.3–5.0
R_K^*	2.8–4.2	1.9–2.9	1.6–2.4	1.4–2.1	1.3–1.9

where c and γ are parameters which can determined using a regression analysis. Considering that $Ra_Q^*/Nu^* = Ek^2 Ra/Pr = Ro_c^2$, where Ro_c is the convective Rossby number (Table 2), Eq. (B.7) can be rewritten as

$$Ro_c^2 = b Ra_Q^{*\,\beta}, \tag{B.8}$$

where $b = 1/c$ and $\beta = 1 - \gamma$. Since $Ra = Ro_c^2 Pr/Ek^2 = b Ra_Q^{*\,\beta} Pr/Ek^2$, we can express the Rayleigh number as follows:

$$Ra = b\frac{\Omega^2 D^4}{\kappa\nu}\left(\frac{1}{4\pi r_o r_i}\frac{\alpha g_o Q}{\rho C_p \Omega^3 D^2}\right)^{\beta}, \tag{B.9}$$

where we assumed that $Q_{adv} \approx Q$.

The diffusivity-free scaling, Eq. (B.7), was derived for rapidly rotating dynamos with $r_i/r_o = 0.35$ (Christensen and Aubert, 2006). Therefore it is questionable whether this kind of scaling can be applied to Titan's ocean which is only weakly affected by rotation, $r_i/r_o \gtrsim 0.8$ and magnetic effects are negligible. In this paper, we determine the bounds of Ra from Eq. (B.9) but with parameters b and β derived from our own dataset. We first convert Ek, Ra, Pr and Nu in Table C.5 to Ro_c and Ra_Q^* and plot the dependence of Ro_c^2 on Ra_Q^* (Fig. B.11) to verify the validity of Eq. (B.8). Using the least squares method, we then obtain $b = 14.73 \pm 0.58$ and $\beta = 0.525 \pm 0.004$. These values correspond to $c = 0.068$ and $\gamma = 0.48$, which do not differ much from the values derived by Christensen and Aubert (2006).

The estimates of Ra obtained from Eq. (B.9) are presented in Table B.3. The admissible values of Ra are found within the interval $\langle 4.5\cdot10^{19}, 10^{22}\rangle$, which lies well within the range of values derived from Eqs. (B.2) and (B.3). It has been argued that the diffusion-free scaling proposed by Christensen and Aubert (2006) is problematic because it is based on simulations where dissipation is far from negligible. According to Cheng and Aurnou (2016), the scaling is likely only valid for the systems where $Ra \sim Ra_{crit}$, i.e. for the heat transfer occurring very near to the onset of convection. If this was the case, the use of Eq. (B.9) in the context of the transitional regime would lead to a significant underestimation of the Rayleigh number. The fact that this approach gives similar values as those obtained independently from Eqs. (B.2) and (B.3) indicates that Eq. (B.9), where $b = 14.73$ and $\beta = 0.525$, can serve as a useful tool when evaluating the Rayleigh number in subsurface oceans of icy moons.

Appendix C. List of simulations

We have performed 83 simulations with free-slip boundary conditions and 32 simulations with no-slip boundary conditions. The basic characteristics of the simulations are summarized in Tables C.4 and C.5. The symbol Re denotes the time-averaged convective Reynolds number (for the definition see Eq. (8) in Amit et al. (2020)), ℓ_{max} is the cut-off degree and N_{rad} is the number of the Chebyshev points. All simulations presented in the paper are available on request.

Table C.4
Results of no-slip simulations.

Model No.	N_{rad}	ℓ_{max}	Pr	Ek	Ra	Nu	Re	q^*	$q^{h/l}$
1n	97	120	1	$1\cdot10^{-4}$	$4.0\cdot10^6$	5.97	208.72	0.44	−0.26
2n	97	120	1	$1\cdot10^{-4}$	$4.4\cdot10^6$	6.28	228.53	0.42	−0.22
3n	97	120	1	$1\cdot10^{-4}$	$5.2\cdot10^6$	7.14	272.14	0.35	−0.17
4n	97	120	1	$1\cdot10^{-4}$	$6.0\cdot10^6$	7.90	306.73	0.32	−0.12
5n	97	120	1	$1\cdot10^{-4}$	$6.8\cdot10^6$	8.75	334.81	0.26	−0.07
6n	97	120	1	$1\cdot10^{-4}$	$7.6\cdot10^6$	9.52	372.68	0.21	−0.03
7n	97	120	1	$1\cdot10^{-4}$	$8.4\cdot10^6$	10.26	407.91	0.18	0.01
8n	97	120	1	$1\cdot10^{-4}$	$9.1\cdot10^6$	10.87	432.71	0.22	0.03
9n	97	130	1	$1\cdot10^{-4}$	$1.1\cdot10^7$	12.17	493.91	0.24	0.06
10n	97	130	1	$1\cdot10^{-4}$	$1.3\cdot10^7$	13.31	557.66	0.27	0.08
11n	97	130	1	$1\cdot10^{-4}$	$1.4\cdot10^7$	13.83	588.17	0.27	0.09
12n	97	130	1	$1\cdot10^{-4}$	$1.6\cdot10^7$	14.65	650.86	0.26	0.09
13n	97	130	1	$1\cdot10^{-4}$	$1.9\cdot10^7$	15.74	714.57	0.26	0.10
14n	97	130	1	$1\cdot10^{-4}$	$2.2\cdot10^7$	16.63	795.72	0.23	0.10
15n	97	130	1	$1\cdot10^{-4}$	$2.5\cdot10^7$	17.42	866.33	0.23	0.09
16n	97	130	1	$1\cdot10^{-4}$	$2.8\cdot10^7$	18.15	919.09	0.22	0.08
17n	97	130	1	$1\cdot10^{-4}$	$3.3\cdot10^7$	19.18	1026.97	0.20	0.08
18n	97	140	1	$1\cdot10^{-4}$	$3.8\cdot10^7$	20.12	1075.46	0.19	0.07
19n	97	120	1	$5\cdot10^{-4}$	$2.1\cdot10^6$	9.30	263.15	0.22	0.04
20n	97	120	1	$5\cdot10^{-4}$	$2.9\cdot10^6$	10.65	317.78	0.19	0.05
21n	97	120	1	$5\cdot10^{-4}$	$3.7\cdot10^6$	11.70	373.34	0.17	0.04
22n	97	120	1	$5\cdot10^{-4}$	$4.4\cdot10^6$	12.52	421.91	0.16	0.03
23n	97	130	1	$5\cdot10^{-4}$	$5.7\cdot10^6$	13.78	486.19	0.13	0.01
24n	97	130	1	$5\cdot10^{-4}$	$7.0\cdot10^6$	14.92	547.64	0.14	0.00
25n	97	140	1	$5\cdot10^{-4}$	$1.1\cdot10^7$	17.64	703.41	0.11	−0.02
26n	97	140	1	$5\cdot10^{-4}$	$1.3\cdot10^7$	18.69	774.82	0.11	−0.03
27n	97	140	1	$5\cdot10^{-4}$	$1.8\cdot10^7$	20.59	908.05	0.11	−0.04
28n	97	120	1	$1\cdot10^{-3}$	$2.3\cdot10^6$	11.04	326.09	0.14	0.01
29n	97	120	1	$1\cdot10^{-3}$	$3.8\cdot10^6$	13.41	430.67	0.10	−0.02
30n	97	120	1	$1\cdot10^{-3}$	$4.8\cdot10^6$	14.43	485.84	0.11	−0.03
31n	97	120	1	$1\cdot10^{-3}$	$6.8\cdot10^6$	16.19	590.23	0.10	0.00
32n	97	120	1	$1\cdot10^{-3}$	$9.8\cdot10^6$	18.20	712.78	0.10	−0.01

Table C.5
Results of free-slip simulations.

Model No.	N_{rad}	ℓ_{max}	Pr	Ek	Ra	Nu	Re	q^*	$q^{h/l}$
1	97	215	1	$1\cdot10^{-5}$	$1.0\cdot10^8$	7.10	1247.33	1.11	−0.32
2	97	215	1	$1\cdot10^{-5}$	$1.7\cdot10^8$	10.52	2153.53	0.90	−0.24
3	97	215	1	$1\cdot10^{-5}$	$2.3\cdot10^8$	14.39	2616.59	0.70	−0.19
4	97	215	1	$1\cdot10^{-5}$	$2.7\cdot10^8$	19.37	2871.43	0.47	−0.07
5	97	215	1	$1\cdot10^{-5}$	$3.0\cdot10^8$	21.01	3500.73	0.41	0.13
6	97	215	1	$1\cdot10^{-5}$	$3.7\cdot10^8$	28.97	4178.88	0.36	0.15
7	97	215	1	$1\cdot10^{-5}$	$4.5\cdot10^8$	39.24	4921.19	0.34	0.21
8	97	120	1	$1\cdot10^{-4}$	$4.0\cdot10^6$	3.22	360.27	0.59	−0.16
9	97	120	1	$1\cdot10^{-4}$	$4.4\cdot10^6$	3.60	396.74	0.44	−0.07
10	97	120	1	$1\cdot10^{-4}$	$5.2\cdot10^6$	3.95	485.07	0.33	0.01
11	97	120	1	$1\cdot10^{-4}$	$6.0\cdot10^6$	4.71	546.20	0.33	0.05
12	97	120	1	$1\cdot10^{-4}$	$6.8\cdot10^6$	5.67	606.49	0.41	0.13
13	97	120	1	$1\cdot10^{-4}$	$7.6\cdot10^6$	6.94	662.77	0.45	0.21
14	97	120	1	$1\cdot10^{-4}$	$8.4\cdot10^6$	8.58	713.20	0.45	0.29
15	97	120	1	$1\cdot10^{-4}$	$9.1\cdot10^6$	9.71	758.09	0.60	0.34
16	97	130	1	$1\cdot10^{-4}$	$1.1\cdot10^7$	11.85	886.62	0.70	0.42
17	97	130	1	$1\cdot10^{-4}$	$1.3\cdot10^7$	13.89	979.09	0.74	0.41
18	97	130	1	$1\cdot10^{-4}$	$1.4\cdot10^7$	14.69	1026.22	0.74	0.41

(continued on next page)

Table C.5 (*continued*).

Model No.	N_{rad}	ℓ_{max}	Pr	Ek	Ra	Nu	Re	q^*	$q^{h/l}$
19	97	130	1	$1{\cdot}10^{-4}$	$1.6{\cdot}10^{7}$	16.46	1105.56	0.69	0.38
20	97	130	1	$1{\cdot}10^{-4}$	$1.9{\cdot}10^{7}$	18.78	1207.74	0.67	0.34
21	97	130	1	$1{\cdot}10^{-4}$	$2.2{\cdot}10^{7}$	21.25	1275.30	0.51	0.31
22	97	130	1	$1{\cdot}10^{-4}$	$2.5{\cdot}10^{7}$	23.60	1346.26	0.50	0.27
23	97	130	1	$1{\cdot}10^{-4}$	$2.8{\cdot}10^{7}$	26.22	1382.94	0.40	0.23
24	97	130	1	$1{\cdot}10^{-4}$	$3.3{\cdot}10^{7}$	29.82	1460.08	0.35	0.22
25	97	140	1	$1{\cdot}10^{-4}$	$3.8{\cdot}10^{7}$	32.77	1703.00	0.34	0.19
26	97	120	1	$5{\cdot}10^{-4}$	$8.8{\cdot}10^{5}$	3.36	244.43	0.70	0.39
27	97	120	1	$5{\cdot}10^{-4}$	$9.8{\cdot}10^{5}$	3.99	256.70	0.65	0.35
28	97	120	1	$5{\cdot}10^{-4}$	$2.1{\cdot}10^{6}$	9.38	398.56	0.34	0.16
29	97	120	1	$5{\cdot}10^{-4}$	$2.9{\cdot}10^{6}$	12.77	473.55	0.33	0.14
30	97	120	1	$5{\cdot}10^{-4}$	$3.7{\cdot}10^{6}$	15.50	534.36	0.29	0.11
31	97	120	1	$5{\cdot}10^{-4}$	$4.4{\cdot}10^{6}$	18.36	610.20	0.24	0.02
32	97	130	1	$5{\cdot}10^{-4}$	$5.7{\cdot}10^{6}$	22.10	685.10	0.26	−0.06
33	97	130	1	$5{\cdot}10^{-4}$	$7.0{\cdot}10^{6}$	24.79	838.93	0.29	−0.09
34	97	140	1	$5{\cdot}10^{-4}$	$1.1{\cdot}10^{7}$	30.77	1217.00	0.27	−0.11
35	97	140	1	$5{\cdot}10^{-4}$	$1.3{\cdot}10^{7}$	33.33	1477.21	0.28	−0.12
36	97	140	1	$5{\cdot}10^{-4}$	$1.8{\cdot}10^{7}$	38.42	1550.83	0.25	−0.13
37	97	120	1	$1{\cdot}10^{-3}$	$2.3{\cdot}10^{6}$	17.36	471.86	0.25	−0.08
38	97	120	1	$1{\cdot}10^{-3}$	$3.8{\cdot}10^{6}$	22.52	666.71	0.27	−0.11
39	97	120	1	$1{\cdot}10^{-3}$	$4.8{\cdot}10^{6}$	25.00	743.68	0.27	−0.12
40	97	120	1	$1{\cdot}10^{-3}$	$6.8{\cdot}10^{6}$	29.00	879.40	0.24	−0.12
41	97	120	1	$1{\cdot}10^{-3}$	$9.8{\cdot}10^{6}$	33.65	1063.69	0.19	−0.11
42	69	159	3	$1{\cdot}10^{-4}$	$4.0{\cdot}10^{6}$	4.22	117.26	1.15	−0.39
43	69	159	3	$1{\cdot}10^{-4}$	$6.0{\cdot}10^{6}$	5.68	170.70	1.05	−0.38
44	69	159	3	$1{\cdot}10^{-4}$	$6.8{\cdot}10^{6}$	6.10	202.00	1.03	−0.36
45	69	159	3	$1{\cdot}10^{-4}$	$8.4{\cdot}10^{6}$	6.79	263.71	0.90	−0.27
46	69	159	3	$1{\cdot}10^{-4}$	$1.1{\cdot}10^{7}$	7.44	369.99	0.67	−0.08
47	76	159	3	$1{\cdot}10^{-4}$	$1.4{\cdot}10^{7}$	10.53	383.92	0.65	−0.07
48	76	159	3	$1{\cdot}10^{-4}$	$1.9{\cdot}10^{7}$	14.55	504.78	0.44	0.13
49	69	159	3	$1{\cdot}10^{-4}$	$2.5{\cdot}10^{7}$	20.64	609.23	0.50	0.25
50	69	159	3	$1{\cdot}10^{-4}$	$3.3{\cdot}10^{7}$	28.17	643.68	0.50	0.23
51	69	159	3	$5{\cdot}10^{-4}$	$2.9{\cdot}10^{6}$	10.96	215.54	0.51	0.20
52	69	159	3	$5{\cdot}10^{-4}$	$3.7{\cdot}10^{6}$	13.65	244.65	0.50	0.19
53	69	159	3	$5{\cdot}10^{-4}$	$4.4{\cdot}10^{6}$	16.37	264.39	0.47	0.18
54	69	159	3	$5{\cdot}10^{-4}$	$5.7{\cdot}10^{6}$	20.24	315.41	0.39	0.13
55	69	159	3	$5{\cdot}10^{-4}$	$7.0{\cdot}10^{6}$	22.00	330.67	0.36	0.14
56	69	159	3	$5{\cdot}10^{-4}$	$1.1{\cdot}10^{7}$	30.90	403.92	0.28	0.04
57	64	159	3	$1{\cdot}10^{-3}$	$2.3{\cdot}10^{6}$	15.41	194.48	0.35	0.13
58	64	147	3	$1{\cdot}10^{-3}$	$3.8{\cdot}10^{6}$	21.98	243.03	0.26	0.04
59	64	147	3	$1{\cdot}10^{-3}$	$4.8{\cdot}10^{6}$	25.63	286.39	0.18	0.00
60	64	147	3	$1{\cdot}10^{-3}$	$6.8{\cdot}10^{6}$	30.93	354.74	0.21	−0.03
61	69	159	10	$1{\cdot}10^{-4}$	$4.0{\cdot}10^{6}$	5.36	26.56	1.28	−0.46
62	69	159	10	$1{\cdot}10^{-4}$	$6.0{\cdot}10^{6}$	7.46	35.71	1.26	−0.44
63	69	159	10	$1{\cdot}10^{-4}$	$6.8{\cdot}10^{6}$	7.96	42.41	1.16	−0.42
64	69	159	10	$1{\cdot}10^{-4}$	$8.4{\cdot}10^{6}$	9.19	51.25	1.08	−0.41
65	69	159	10	$1{\cdot}10^{-4}$	$1.1{\cdot}10^{7}$	11.03	70.21	0.99	−0.38
66	69	159	10	$1{\cdot}10^{-4}$	$1.4{\cdot}10^{7}$	13.09	83.45	0.95	−0.37
67	69	159	10	$1{\cdot}10^{-4}$	$1.9{\cdot}10^{7}$	16.14	111.02	0.82	−0.31
68	81	159	10	$1{\cdot}10^{-4}$	$2.5{\cdot}10^{7}$	18.84	175.25	0.70	−0.21
69	69	159	10	$1{\cdot}10^{-4}$	$3.3{\cdot}10^{7}$	23.47	224.16	0.58	−0.15
70	69	159	10	$5{\cdot}10^{-4}$	$2.1{\cdot}10^{6}$	10.29	50.27	0.53	−0.13
71	69	159	10	$5{\cdot}10^{-4}$	$2.9{\cdot}10^{6}$	13.24	57.39	0.45	−0.07
72	69	159	10	$5{\cdot}10^{-4}$	$3.7{\cdot}10^{6}$	15.39	80.57	0.41	−0.01
73	69	159	10	$5{\cdot}10^{-4}$	$4.4{\cdot}10^{6}$	17.56	93.56	0.36	0.04
74	65	159	10	$5{\cdot}10^{-4}$	$5.7{\cdot}10^{6}$	21.24	103.41	0.29	0.07
75	69	159	10	$5{\cdot}10^{-4}$	$7.0{\cdot}10^{6}$	24.24	116.48	0.33	0.09
76	69	159	10	$5{\cdot}10^{-4}$	$1.1{\cdot}10^{7}$	30.77	153.27	0.34	0.12
77	65	147	10	$1{\cdot}10^{-3}$	$2.3{\cdot}10^{6}$	16.13	72.62	0.32	0.08
78	65	159	10	$1{\cdot}10^{-3}$	$3.8{\cdot}10^{6}$	22.20	90.79	0.34	0.09
79	65	159	10	$1{\cdot}10^{-3}$	$4.8{\cdot}10^{6}$	25.31	98.39	0.31	0.10
80	65	159	10	$1{\cdot}10^{-3}$	$6.8{\cdot}10^{6}$	30.39	119.13	0.29	0.08
81	73	186	10	$1{\cdot}10^{-3}$	$1.1{\cdot}10^{7}$	38.21	339.68	0.23	0.03
82	73	186	10	$1{\cdot}10^{-3}$	$1.6{\cdot}10^{7}$	46.43	350.49	0.17	0.01
83	73	186	10	$1{\cdot}10^{-3}$	$2.1{\cdot}10^{7}$	50.43	374.25	0.17	−0.01

References

Agrusta, R., Morison, A., Labrosse, S., Deguen, R., Alboussière, T., Tackley, P.J., Dubuffet, F., 2020. Mantle convection interacting with magma oceans. Geophys. J. Int. 220, 1878–1892.

Amit, H., Choblet, G., Tobie, G., Terra-Nova, F., Čadek, O., Bouffard, M., 2020. Cooling patterns in rotating thin spherical shells - Application to Titan's subsurface ocean. Icarus 338, 113509.

Aubert, J., 2005. Steady zonal flows in spherical shell fluid dynamos. J. Fluid. Mech. 542, 53–67.

Aurnou, J.M., Heimpel, M., Wicht, J., 2007. The effects of vigorous mixing in a convective model of zonal flow on the ice giants. Icarus 190, 110–126.

Barr, A.C., McKinnon, W.B., 2007. Convection in ice I shells and mantles with self-consistent grain size. J. Geophys. Res. 112, 2012.

Běhounková, M., Tobie, G., Choblet, G., Čadek, O., 2013. Impact of tidal heating on the onset of convection in Enceladus's ice shell. Icarus 226, 898–904.

Běhounková, M., Tobie, G., Choblet, G., Kervazo, M., Daswani, M.M., Dumoulin, C., Vance, S.D., 2021. Tidally induced magmatic pulses on the oceanic floor of Jupiter's moon Europa. Geophys. Res. Lett. 48, e2020GL090077.

Čadek, O., Kalousová, K., Kvorka, J., Sotin, C., 2021. The density structure of Titan's outer ice shell. Icarus 364, 114466.

Čadek, O., Souček, O., Běhounková, M., 2019a. Is Airy isostasy applicable to icy moons? Geophys. Res. Lett. 46, 14, 299–14, 306.

Čadek, O., Souček, O., Běhounková, M., Choblet, G., Tobie, G., Hron, J., 2019b. Long-term stability of Enceladus' uneven ice shell. Icarus 319, 476–484.

Cheng, J.S., Aurnou, J.M., 2016. Tests of diffusion-free scaling behaviors in numerical dynamo datasets. Earth Planet. Sci. Lett. 436, 121–129.

Cheng, J.S., Aurnou, J.M., Julien, K., Kunnen, R.P.J., 2018. A heuristic framework for next-generation models of geostrophic convective turbulence. Geophys. Astrophys. Fluid Dyn. 112, 277–300.

Choblet, G., Tobie, G., Sotin, C., Kalousová, K., Grasset, O., 2017a. Heat transport in the high-pressure ice mantle of large icy moons. Icarus 285, 252–262.

Choblet, G., Tobie, G., Sotin, M., Čadek, O., Postberg, F., Souček, O., 2017b. Powering prolonged hydrothermal activity inside Enceladus. Nat. Astr. 1, 841–847.

Choukroun, M., Sotin, C., 2012. Is Titan's shape caused by its meteorology and carbon cycle? Geophys. Res. Lett. 39, L04201.

Christensen, U.R., 2002. Zonal flow driven by strongly supercritical convection in rotating spherical shells. J. Fluid Mech. 470, 115–133.

Christensen, U.R., Aubert, J., 2006. Scaling properties of convection-driven dynamos in rotating spherical shells and application to planetary magnetic fields. Geophys. J. Int. 166, 97–114.

Corlies, P., Hayes, A.G., Birch, S.P.D., Lorenz, R., Stiles, B.W., Kirk, R., Poggiali, V., Zebker, H., Iess, L., 2017. Titan's topography and shape at the end of the Cassini mission. Geophys. Res. Lett. 44, 11754–11761.

Durante, D., Hemingway, D.J., Racioppa, P., Iess, L., Stevenson, D.J., 2019. Titan's gravity field and interior structure after Cassini. Icarus 326, 123–132.

Ecke, R.E., Niemela, J.J., 2014. Heat transport in the geostrophic regime of rotating Rayleigh-Bénard convection. Phys. Rev. Lett. 113, 114301.

Gastine, T., Wicht, J., Arnou, J.M., 2015. Turbulent Rayleigh-Bénard convection in spherical shells. J. Fluid Mech. 778, 721–764.

Gastine, T., Wicht, J., Aubert, J., 2016. Scaling regimes in spherical shell rotating convection. J. Fluid Mech. 808, 690–732.

Gilman, P.A., 1977. Nonlinear dynamics of Boussinesq convection in a deep rotating spherical shell-i. Geophys. Astrophys. Fluid Dyn. 8, 93–135.

Guervilly, C., Cardin, P., 2017. Multiple zonal jets and convective heat transport barriers in a quasi-geostrophic model of planetary cores. Geophys. J. Int. 211, 455–471.

Julien, K., Knobloch, E., Rubio, A.M., Vasil, G., 2012a. Heat transport in low-Rossby-number Rayleigh-Bénard convection. Phys. Rev. Lett. 109, 254503.

Julien, K., Rubio, A.M., Grooms, I., Knobloch, E., 2012b. Statistical and physical balances in low Rossby number Rayleigh-Bénard convection. Geophys. Astrophys. Fluid Dyn. 106, 392–428.

Kalousová, K., Sotin, C., 2020. The insulating effect of methane clathrate crust on Titan's thermal evolution. Geophys. Res. Lett. 47, e2020GL087481.

Kihoulou, M., Čadek, O., Kalousová, K., Choblet, G., 2021. Effect of ocean heat flux on Titan's topography and tectonic stresses. In: European Planetary Science Congress 2021, 13–24 2021, EPSC2021-155.

King, E.M., Aurnou, J.M., 2013. Turbulent convection in liquid metal with and without rotation. Proc. Natl. Acad. Sci. USA 110, 6688–6693.

King, E.M., Soderlund, K.M., Christensen, U.R., Wicht, J., Aurnou, J.M., 2010. Convective heat transfer in planetary dynamo models. Geochem. Geophys. Geosyst. 11, Q06016.

Kuang, W.L., Bloxham, J., 1997. An Earth-like numerical dynamo model. Nature 389, 371–374.

Kuang, W.L., Bloxham, J., 1999. Numerical modeling of magnetohydrodynamic convection in a rapidly rotating spherical shell: Weak and strong field dynamo action. J. Comput. Phys. 153, 51–81.

Kvorka, J., Čadek, O., Tobie, G., Choblet, G., 2018. Does Titan's long-wavelength topography contain information about subsurface ocean circulation dynamics? Icarus 310, 149–164.

Labrosse, S., Morison, A., Deguen, R., Alboussière, T., 2018. Rayleigh-Bénard convection in a creeping solid with melting and freezing at either or both its horizontal boundaries. J. Fluid Mech. 846, 5–36.

Lobo, A.H., Thompson, A.F., Vance, S.D., Tharimena, S., 2021. A pole-to-equator ocean overturning circulation on Enceladus. Nat. Geosci. 14, 185–189.

Martinec, Z., 1989. Program to calculate the spectral harmonic expansion coefficients of the two scalar fields product. Comput. Phys. Comm. 54, 177–182.

Moore, J.M., Pappalardo, R.T., 2011. Titan: An exogenic world? Icarus 212, 790–806.

Morison, A., Labrosse, S., Deguen, R., Alboussière, T., 2019. Timescale of overturn in a magma ocean cumulate. Earth Planet. Sci. Lett. 516, 25–36.
Nimmo, F., Pappalardo, R.T., 2016. Ocean worlds in the outer solar system. J. Geophys. Res.-Planets 121, 1378–1399.
Olson, P., Christensen, U.R., 2002. The time-averaged magnetic field in numerical dynamos with non-uniform boundary heat flow. Geophys. J. Int. 151, 809–823.
Olson, P., Christensen, U., Glatzmaier, G.A., 1999. Numerical modeling of the geodynamo: Mechanisms of field generation and equilibration. J. Geophys. Res.-Solid Earth 104, 10383–10404.
Roberts, P.H., King, E.M., 2013. On the genesis of the Earth's magnetism. Rep. Progr. Phys. 76, 096801.
Schaeffer, N., 2013. Efficient spherical harmonic transforms aimed at pseudospectral numerical simulations. Geochem. Geophys. Geosyst. 14, 751–758.
Soderlund, K.M., 2019. Ocean dynamics of outer solar system satellites. Geophys. Res. Lett. 46, 8700–8710.
Soderlund, K.M., Heimpel, M.H., King, E.M., Aurnou, J.M., 2013. Turbulent models of ice giant internal dynamics: Dynamos, heat transfer, and zonal flows. Icarus 224, 97–113.
Soderlund, K.M., Schmidt, B.E., Wicht, J., Blankenship, D.D., 2014. Ocean-driven heating of Europa's icy shell at low latitudes. Nat. Geosci. 7, 16–19.
Vance, S., Panning, M.P., Stahler, S., Cammarano, F., Bills, B.G., Tobie, G., Kamata, S., Kedar, S., Sotin, C., Pike, W.T., Lorenz, R., Huang, H.H., Jackson, J.M., Banerdt, B., 2018. Geophysical investigations of habitability in ice-covered ocean worlds. J. Geophys. Res.-Planets 123, 180–205.
Yadav, R., Gastine, T., Christensen, U., Duarte, L., Reiners, A., 2016. Effect of shear and magnetic field on the heat-transfer efficiency of convection in rotating spherical shells. Geophys. J. Int. 204, 1120–1133.
Zeng, Y., Jansen, M.F., 2021. Ocean circulation on Enceladus with a high- versus low-salinity ocean. Planet. Sci. J. 2, 151.
Zhang, K., Jones, C.A., 1993. The influence of Ekman boundary layers on rotating convection. Geophys. Astroph. Fluid Dyn. 71, 145–162.